UPPSALA
UNIVERSITET

Digital Comprehensive Summaries of Uppsala Dissertations from the Faculty of Science and Technology 1360

Constructing and Commissioning HELIOS – A High Harmonic Generation Source for Pump-Probe Measurements with sub 50 fs Temporal Resolution

The Development of Experimental Equipment for Extreme Ultraviolet Spectroscopy

JOACHIM A. TERSCHLÜSEN

ACTA
UNIVERSITATIS
UPSALIENSIS
UPPSALA
2016

ISSN 1651-6214
ISBN 978-91-554-9528-2
urn:nbn:se:uu:diva-281298

Dissertation presented at Uppsala University to be publicly examined in Häggsalen, Ångströmlaboratoriet, Lägerhyddsvägen 1, Uppsala, Tuesday, 17 May 2016 at 13:15 for the degree of Doctor of Philosophy. The examination will be conducted in English. Faculty examiner: Professor Margaret Murnane (University of Colorado).

Abstract
Terschlüsen, J. A. 2016. Constructing and Commissioning HELIOS – A High Harmonic Generation Source for Pump-Probe Measurements with sub 50 fs Temporal Resolution. The Development of Experimental Equipment for Extreme Ultraviolet Spectroscopy. *Digital Comprehensive Summaries of Uppsala Dissertations from the Faculty of Science and Technology* 1360. 80 pp. Uppsala: Acta Universitatis Upsaliensis. ISBN 978-91-554-9528-2.

This thesis presents HELIOS, an in-house laboratory for time-resolved pump-probe spectroscopy with extreme-ultraviolet (XUV) probe radiation. A wide span of pump wavelengths can be generated using commercial laser equipment while XUV probe radiation is generated via a high harmonic generation process in a noble gas delivering probe photons with energies between 20 eV and 72 eV. The XUV beam path features a time-preserving monochromator and was constructed and built in-house. HELIOS features an overall time resolution of about 50 fs when using 800 nm pump and 41 eV probe photons. An energy resolution of 110 meV at 41 eV photon energy can be achieved. HELIOS features two beamlines. One μ-focus beamline with an XUV focal size of about 20 μm can be used with experiments that require such a small XUV focal size as well as with different end stations. The other beamline features a semi-permanently mounted end station for angle-resolved photoelectron spectroscopy under ultra-high vacuum conditions.

Experiments demonstrating the usability of HELIOS and the two beamlines are presented. A pump-probe measurement on graphene demonstrates the capability of determining a large part of the k-space in only one measurement due to the use of an ARTOF angle-resolved time-of-flight electron spectrometer. A non-angle-resolved pump-probe measurement on the conducting polymer PCPDTBT demonstrates the high signal-to-noise ratio achievable at this beamline in non-angle-resolved photoelectron-spectroscopy pump-probe measurements. The usability of the μ-focus beamline is demonstrated with time-resolved measurements on magnetic samples employing an in-house-designed spectrometer. These experiments allow the retrieval of element-specific information on the magnetization within a sample employing the transversal magneto-optical Kerr effect (T-MOKE).

Additionally, a Fourier transform spectrometer for the XUV is presented, the concept was tested at a synchrotron and it was used to determine the longitudinal coherence of the XUV radiation at HELIOS.

Keywords: Angle-resolved photoemission spectroscopy, Angle resolved photoemission spectroscopy, Angle-resolved time-of-flight, Angle resolved time of flight, ARTOF, ARPES, tr-ARPES, fs, fs resolution, Fourier transform spectrometer, Fourier-transform spectrometer, Fourier transform spectroscopy, Fourier-transform spectroscopy, FTS, gas cell, high harmonic generation, laser, liquid jet, monochromator, HELIOS, HHG, off-plane mount, off plane mount, OPA, optical parametric amplifier, PCPDTBT, pulse shaping, pump probe, pump-probe measurements, pump-probe measurements, pump-probe spectroscopy, pump-probe spectroscopy, Rowland spectrometer, time-of-flight spectrometer, time of flight spectrometer, TOF, time-resolved spectroscopy, time resolved spectroscopy, time-resolved experiments, time resolved experiments, T-MOKE, tr-PES, PES, photoelectron spectroscopy, transverse magneto optical Kerr effect, transverse magneto-optical Kerr effect, ultrafast, ultra-high vacuum, ultra high vacuum, UHV, XUV, VUV, X-rays, Permalloy, magnetization dynamic

Joachim A. Terschlüsen, Department of Physics and Astronomy, Molecular and condensed matter physics, Box 516, Uppsala University, SE-751 20 Uppsala, Sweden.

ISSN 1651-6214
ISBN 978-91-554-9528-2
urn:nbn:se:uu:diva-281298 (http://urn.kb.se/resolve?urn=urn:nbn:se:uu:diva-281298)

This thesis is dedicated to those
who have worked or will work with HELIOS.

List of Papers

This thesis is based on the following papers, which are referred to in the text by their Roman numerals.
Reprints were made with permission from the respective publishers.

I **Spectroscopy in the vacuum-ultraviolet**
M. Agåker, J. Andersson, J.C. Englund, J. Rausch, J.-E. Rubensson and J. Nordgren
Nature Photonics, Vol. **5**, (2011), p. 248

II **Measuring the temporal coherence of a high harmonic generation setup employing a Fourier transform spectrometer for the VUV/XUV**
J.A. Terschlüsen, M. Agåker, M. Svanqvist, S. Plogmaker, J. Nordgren, J.-E. Rubensson, H. Siegbahn and J. Söderström
Nuclear Instruments and Methods in Physics Research A, Vol. **768**, (2014), pp. 84-88

III **HELIOS–A laboratory based on high-order harmonic generation of extreme ultraviolet photons for time-resolved spectroscopy**
S. Plogmaker, J.A. Terschlüsen, N. Krebs, M. Svanqvist, J. Forsberg, U.B. Cappel, J.-E. Rubensson, H. Siegbahn and J. Söderström
Review of Scientific Instruments, Vol. **86**, (2015), pp. 123107-1–9

IV **Direct measurement of excited electrons in a low bandgap polymer using XUV based time-resolved photoelectron spectroscopy**
U.B. Cappel, S. Plogmaker, J.A. Terschlüsen, T. Leitner, E.M.J. Johansson, T. Edvinsson, A. Sandell, O. Karis, H. Siegbahn, S. Svensson, N. Mårtensson, H. Rensmo and J. Söderström
Submitted to NPG Asia Materials

V **A Setup for Element Specific Magnetization Dynamics using the Transverse Magneto-Optic Kerr Effect in the energy range of 35-70 eV**
S. Jana, J.A. Terschlüsen, R. Stefanuik, S. Pogmaker, S. Troisi, J. Söderström, O. Karis
Manuscript

Comments on my personal contribution

All the work presented in this thesis is a result of joint efforts of many people, which is reflected in the author lists. (Note that my former family name Rausch is used in the first publication.)

Paper I: I took part in preparing the beamtime and participated as one of two persons at the beamtime itself. I did one out of two data analyses which were done to gain confidence in the results.

Paper II: I was a main person in the preparation of the experiments and the experiments themselves. Data analysis and writing were done by me.

Paper III: This paper is without doubts the paper which represents the biggest achievement during my PhD studies. The laser system was purchased and the drawings for the gas-cell chamber, the monochromator and the beam-routing chamber were done before I started to work with HELIOS. From that point on I was one of the main responsible persons in the buildup and commissioning of the laboratory. I was a main person in designing the refocusing chamber of the UHV beamline and in all measurements needed for this paper. The writing was done together with Dr. S. Plogmaker.

Paper IV: I was one of the main persons in preparing the equipment and in performing the measurements and I wrote essential parts of the software needed to perform automated delay scans.

Paper V: I was one of the main responsible persons in designing the T-MOKE spectrometer and its data acquisition software. I participated in all the measurements and supervised part of their analysis. I did a main part of the writing.

Contents

Abbreviations and acronyms

ARPES	Angle-Resolved Photoemission Spectroscopy
ARTOF	Angle-Resolved Time-of-Flight
FEL	Free-Electron Laser
fs	Femtosecond ($1 \cdot 10^{-15}$ s)
FTS	Fourier Transform Spectrometer
FWHM	Full Width at Half Maximum
HELIOS	High Energy Laser Induced Overtone Source
HHG	High Harmonic Generation
ns	Nanosecond ($1 \cdot 10^{-9}$ s)
MCP	Micro-Channel Plate
OPA	Optical Parametric Amplifier
OPD	Optical Path Difference
PCPDTBT	poly[2,6-(4,4-bis-(2-ethylhexyl)-4*H*-cyclopenta [2,1-*b*;3,4-*b′*]dithiophene)-*alt*-4,7(2,1,3-benzothiadiazole)]
PES	Photoelectron Spectroscopy
ps	Picosecond ($1 \cdot 10^{-12}$ s)
Regen	Regenerative Amplification Stage
SASE	Self-Amplified Spontaneous Emission
Ti:sapphire	Titanium:sapphire
TOF	Time-of-Flight
TR-PES	Time-Resolved Photoelectron Spectroscopy
T-MOKE	Transverse Magneto-Optic Kerr Effect
UHV	Ultra-High Vacuum
UV	Ultraviolet
VUV	Vacuum Ultraviolet
XUV	Extreme Ultraviolet

1 Introduction and background

1.1 The benefits of time-resolved spectroscopy

A huge variety of different techniques can be gathered under the term spectroscopy. Spectroscopy is used to obtain information about matter by analyzing electromagnetic radiation and can be used for a multitude of different applications. Its history reaches back to the time of Newton and its significance for the history of science can hardly be underestimated. Over the years, more and more spectroscopic techniques were developed aiming on the study of objects of different sizes ranging from whole galaxies to single atoms and with different energies ranging from gamma rays to radio waves.

However, spectroscopy has, for the very most of the time, been a technique which only allowed studying a steady state of an object or sample. It was typically not able, to deliver information about how processes actually happen (e.g. solar harvesting, photo-dissociation of molecules, phase transitions). Therefore, scientists were dependent on creating models that bridge the gap between a known initial state of a process and its known final state. The actual *dynamics* of how an initial state evolves into the final state could not be observed. Although using models is mostly possible, it is not always a satisfying approach and might sometimes also fail in describing what actually happens.

A crash test for cars without slow-motion cameras might be an easier accessible analogy for this situation. One knows the car and the initial conditions very well, one also knows the result after the crash but if one lacks the slow-motion pictures one misses the dynamics of the impact. Hence, one can try to model the impact to finally make the model look like the result of the crash. However, if this is not successful, one might just have missed some physics and it will be hard to find a fix for this problem. Even if this final state of the modeling is looking as in reality it does not necessarily mean that the dynamics were described correctly. As a workaround to this problem, one can try to constantly illuminate the crash scene and take one image with a very long shutter time. All the dynamics would be captured but in only one image. However, this image might then only allow following traces of torn off fragments. The actual impact dynamics are still missing, although, it is precisely the control over these dynamics which is a major design goal for a car.

Now, if one chooses a more scientific example showing the same principle, one might look at a solar-cell sample. Scientist can provide rather precise descriptions of e.g. the electronic structure of a solar cell in the dark. If one illuminates the solar cell one can in principle measure all the excited states which electrons reach when the solar cell is exposed to light, meaning all the dynamics at once, as one could capture the crash-test dynamics in only one image. However, the use of a solar cell lies precisely in the electron dynamics caused when exposed to light. A solar cell might be unusable if it features the wrong electron dynamics even if it otherwise has good conditions for high efficiency. As for a crash test one might try to model these dynamics, relying on the feasibility and quality of the modeling. However, as slow-motion cameras might provide important information about crash-test dynamics, time-resolved spectroscopy might provide important information about the dynamics in a certain process or sample as e.g. in a solar cell.

1.2 Pump-probe spectroscopy

One can find examples of time-resolved spectroscopy dating back to 1950.[1] However, the time resolution in that case was 500 nanoseconds (ns) ($500 \cdot 10^{-9}$ s) while time resolutions in the femto- (10^{-15} s) or even attoseconds (10^{-18} s) are achieved today.[2] A significant part of these advances were made possible by a rapid development of laser technology and finally the development of ultrafast pulsed lasers. These are commonly used to perform so-called pump-probe measurements. This means that one achieves time resolution by using two extremely short light pulses with an adjustable delay, as shown in *Figure 1*.

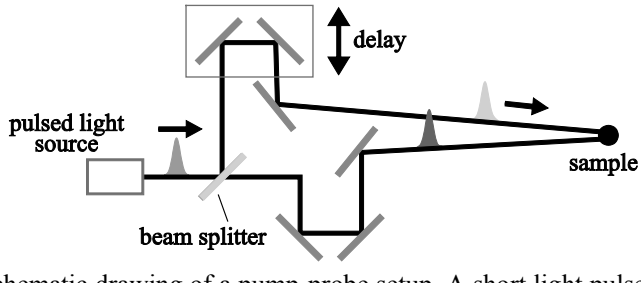

Figure 1. Schematic drawing of a pump-probe setup. A short light pulse is split by a beam splitter, creating a pump and a probe pulse. The probe pulse travels a longer path and is hence delayed. Thereafter it is used to probe the sample which was before pumped by the pump pulse. [own work, published under CC0 license][3]

The first pulse is called pump pulse and is used to excite the sample. In the case of a solar cell, the pump pulse would excite electrons from the ground state to excited states, as it would also be done by the illumination with sunlight. The second pulse is called probe pulse and is used to probe the sample after a certain time delay. One can thereby measure in which states the excited electrons are at that time. Doing this with a set of different delays allows monitoring the dynamics of the sample initiated by the pump pulse. The shorter the light pulses the better time resolution can be achieved. This is similar to achieving less in-motion blur when taking a photo with a flash in contrast to taking a photo with a long exposure time without flash. The result of such a measurement series could be compared with a set of images of how the solar cell, or more general a sample, reacted to the pump pulse. Such a series monitors the dynamics of a process as a slow-motion video consisting of many images monitors impact dynamics in a crash test.

Although it might seem that an excitation of a sample with a light pulse limits this technique to processes that are in anyway connected to the absorption of light, pump-probe measurements are used to perform measurement in a huge variety of different areas. The reason for this is that photons can also be used to deposit energy in a system and thereby to e.g. heat a sample, to cause a phase transition, to change the samples magnetization, to trigger chemical reactions or to excite vibrations in molecules as well as to dissociate them.

1.3 Extending the photon-energy range

Although time-resolved spectroscopy with lasers developed into many different directions and became a very handy tool for a lot of scientists, it was for long times limited by the energies that could be achieved with laser pulses. A way of converting laser light in the infrared (IR) or visible to wavelength in the vacuum ultraviolet (VUV), extreme ultraviolet (XUV) or even up to soft x-rays was already found in 1987 by means of so-called high harmonic generation (HHG).[4] However, its use in spectroscopic applications was rather limited. Photons with energies above the ultra violet (UV) were rather generated by helium lamps,[5] x-ray tubes and synchrotrons. This made those energies rather unreachable for time-resolved spectroscopy with femtosecond (fs) time resolution as the mentioned sources could not provide fs pulses.

Within the last two decades, this situation changed by the emergence of new techniques as femto slicing at synchrotrons or new concepts like free-electron lasers (FELs) which are described briefly in Section 3.1. However, the access to these techniques is rather limited, which causes a rather stringent working environment while the small number of these facilities often means that they are mostly far away. Meanwhile, ultrafast commercial lasers

got powerful and reliable enough to make high harmonic generation a useful tool for ultrafast spectroscopy with energies above the UV region. Today, such a light source can be built as a stable table-top setup, while leaving experimental and financial margins to combine it with experimental equipment needed for time-resolved spectroscopy. Not least the home-lab character of these sources lets them be a valuable complement to the large facilities described above.

2 This thesis in context

The main work within my thesis was to build and commission a laboratory for time-resolved spectroscopy which uses XUV radiation created from an ultrafast laser pulse via an HHG process. The laboratory is called HELIOS, which is an acronym for "High Energy Laser Induced Overtone Source" and was built within the division of Molecular and Condensed Matter Physics at the department of Physics and Astronomy at Uppsala University. This division features a very broad research reaching from surface science on single crystals, organic solar cells, biomolecules and spectroscopy on liquids to gases and magnetism. Hence, one of the key parameters for HELIOS is to be very flexible when it comes to its usability and the kind of research conducted with it.

The division of Molecular and Condensed Matter Physics also features a strong tradition of developing and constructing new instruments for scientific applications. One example for this is the development of a concept-test Fourier transform spectrometer (FTS) for the XUV region,[6] which was developed trying to push the wavelength limit of Fourier transform spectroscopy towards shorter wavelengths into the XUV. A part of my thesis deals with testing this new spectrometer and exploring its capabilities and limitations.

3 Experimental techniques

This chapter describes some techniques relevant for this thesis as well as some alternative techniques which might be used for similar research. However, the descriptions will concentrate only on the basic principles and more detailed descriptions can be found in the references.

3.1 Optically-driven time-resolved techniques

All techniques described in the following subsections are techniques that can be used in a pump-probe scheme as described in the introduction Section 1.2. Besides the fact that also HELIOS employs the pump-probe scheme, the reason for this is that pump-probe measurements are widely used and allow for gaining time-resolved data from a large variety of different samples in different scientific areas. An advantageous feature of the pump-probe scheme is that the time resolution is, to a high degree, dependent on the light source and increases with shorter pump and probe pulses and a higher stability of their delay. In addition, it is possible to perform different experiments with the same light source while the spectrometers used (e.g. photon- or electron spectrometers) do not have an impact on the overall temporal resolution. This particularly allows using standard spectrometers already developed for non time-resolved measurements.

Each of the different time-resolved techniques described in the following subsections are a topic on their own. The descriptions given here aim on comparing these different approaches from a user perspective and are, hence, rather general. This focus and briefness means that there are hardly statements without exceptions.

3.1.1 Laser-laser pump probe

Since the demonstration of the first laser, laser technology progressed very fast. The spectrum of available beam powers, pulse lengths and wavelengths has been increasing for decades. Laser-laser pump probe is a rather simple technique which can be fitted in one room and requires rather little upkeep. Ultrafast pulsed lasers with pulse lengths down to a few femtoseconds are available and can be easily handled and characterized by the use of standard optical equipment. A laser beam can easily be split into a pump- and probe

beam by means of a beam splitter. Using a retroreflector on a delay stage in one of the two beam paths allows setting a precise time delay between both pulses. As the time delay is dependent on the path-length difference between the two beams it is rather simple to set and keep a certain delay with little jitter. Absolute time differences of the driving laser are not of relevance in this configuration since both pump- and probe pulse originate from the same laser pulse. Moreover, it is possible to vary the wavelength of the laser radiation by using a tunable laser or to continuously change the wavelength by means of nonlinear optics (see Ref. 7 and references therein). This makes pump-probe setups with variable pump- and/or probe wavelengths possible. However, the photon energies of lasers are limited to a region reaching from the far infrared to the ultraviolet. Higher photon energies cannot be achieved by using standard laser equipment since photons in the vacuum ultraviolet (VUV) are absorbed by all kind of different materials as well as in air.

Altogether, laser-laser pump probe is a very versatile and easy to use tool for a home lab with high repetition rates up to ≥100 kHz,[8,9] little jitter and very good time resolution down to a few femtoseconds. The main disadvantage is the very limited probe photon energy, which does only allow for probing the valence band of a sample.

3.1.2 High harmonic generation

As discussed above (Subsection 3.1.1), the main limitation of laser-laser pump probe is the limited wavelength/energy of the probe pulse. This can be overcome by generating high harmonics, usually done by focusing a femtosecond laser pulse into a noble gas. That way, odd overtones of the driving laser frequency are generated easily surpassing 70 eV in energy.[10] Even high harmonics forming a supercontinuum that covers the water window from 280 eV to 530 eV have been demonstrated.[11] However, the number of high harmonic photons is drastically smaller than the one from the used driving laser pulse as the conversion efficiency is about 10^{-5} or lower.[11]

XUV radiation is absorbed very strongly in air, which means that the whole XUV beam path including the sample has to be kept under vacuum. This adds a lot of complexity and cumbersomeness compared to laser-laser pump probe. The significantly higher probe-photon energies, however, allow for probing the full valence-electronic structure and some shallow core levels, partly even with element specificity (compare also Section 3.3). Higher photon energies also enable angle-resolved photoelectron spectroscopy and band mapping with access to much larger parts of the k-space, while the coherence of the light allows diffractive imaging.[12,13]

HHG pump probe can be seen as an extension of laser-laser pump probe allowing for different kind of experiments due to the higher probe energies. Furthermore, very short probe pulses with lengths in the low attoseconds can be achieved.[10] This comes at the price of a more complex and costly system,

the need of more intense laser pulses, which practically limits the repetition rate, and the need to keep the probe beam path under vacuum. The latter complicates the general setup as well as well as the handling of samples as objects in vacuum are much harder to control and access. The access to some classes of samples, like liquids, is even limited as they are in principle incompatibility to vacuum. Additionally, the high absorption of high harmonic photons in basically all materials makes this method very surface sensitive (compare Section 3.3). The non-continues HHG spectrum, consisting only of discrete peaks can also be a disadvantage compared to spectroscopy at synchrotrons or free-electron lasers since it makes resonant excitations rather difficult. Nevertheless, high harmonic generation is a technique that is currently developing very rapidly towards a cost-efficient home-lab solution for the generation of very short and coherent pulses in the VUV to X-ray region.

3.1.3 Laser-pump x-ray-probe at synchrotrons

Synchrotrons provide high brilliance, very good energy resolution and a wide range of accessible energies, while delivering photon pulses with pulse lengths in the picosecond (ps) regime. However, their pulses in normal operation are spaced so close (e.g. 2 ns)[14] that it might be very difficult to directly use them for pump-probe spectroscopy. Reasons can be that there might not be a pump laser available featuring such high repetition rates as 500 MHz,[14] the sample might simply not stand that many pump and probe pulses per second or there might not be time for the observed system to decay back into its ground state. Another reason, especially when using time-of-flight spectrometers is that the spectrometer itself might not be able to handle that high repetition rates.

In these cases, it might be necessary to reduce the repetition rate of the synchrotron pulses delivered to the experiment. There are different approaches to this problem. A straight forward solution is a chopper system (see Ref. 15 and references therein), which only transmits a fraction of the pulses, thereby reducing the repetition rate. However, depending on the degree of demands put on it, a chopper system can become very complex. Problems might arise from the required synchronization of the chopper with the light source, the impact of the radiation onto the chopper as well as its mechanical stability.

Another approach would be to limit the repetition rate with which the synchrotron produces photon pulses. A way of doing this is to run the synchrotron in a so-called single-bunch mode. However, this strongly affects other users of such facilities as it comes along with a rather limited photon flux, which is why beamtime with such an operation mode is rare. Newly developed techniques, though, allow for lower repetition rates at one beamline while leaving other users unaffected.[16,17]

Laser-pump x-ray-probe is a technique which has its advantages in the large energy range of synchrotron pulses, which spans from the microwaves to the hard x-rays. This allows a complete determination of the electronic structure of the sample, if desired, at the same time, using the very good energy resolution of the x-ray photons. As these experiments can only be conducted at specially equipped beamlines of synchrotrons, their accessibility is limited. Further shortcomings are the rather poor time resolution which is limited by the pulse length of the x-ray pulse from the synchrotron to about 30 ps to 3 ps[14,17,18] and the need of synchronizing the pump laser to the x-ray pulse. Hereby, the fact that both pulses are of completely different origin introduces additional jitter. To work around these problems, femto slicing[18,19] is currently introduced at an increasing number of synchrotrons.

3.1.3.1 Femto slicing

Femto slicing is used to increase the time resolution in laser-pump x-ray-probe experiments. In general, a synchrotron generates light by letting a near-speed-of-light electron bunch pass through a magnetic structure such as a wiggler or undulator.[20] Since the electron bunches have a length of about 30 ps to 100 ps (full width at half maximum (FWHM))[18] the radiation emitted by them features similar pulse lengths. The idea of femto slicing is to use a femtosecond laser pulse to modulate the energy of an electron slice within an electron bunch as shown in *Figure 2*.[19] For that, the electron bunch is sent through a wiggler or undulator, which causes the electrons to emit light. The wavelength of the emitted light is set so that it fits the wavelength of a femtosecond laser pulse which is sent through the wiggler or undulator simultaneous with the electron bunch. This laser pulse then modifies the energy of the co-propagating electrons in its electric field. This allows separating the electrons by means of a bending magnet, based on their different kinetic energies. Afterwards, this sliced bunch can be send through a normal undulator whereupon the sliced part of the bunch emits radiation in a slightly different direction and with a pulse length similar to the one of the laser pulse. This allows pulse lengths of about 100 fs at the experiment.[18]

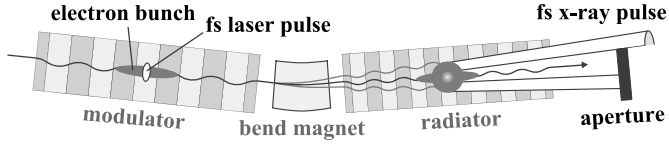

Figure 2. Schematic drawing a femto-slicing setup. The electron bunch and laser pulse enter the modulator from the left. The energy within a slice of electrons is altered by the fs laser pulse, leading to a different trajectory of those electrons through the bend magnet. This altered electron slice then emits a short x-ray pulse passing the aperture to the beamline while the ordinary radiation is blocked. [Reprinted figure with permission from Ref. 18. Copyright 2016 by the American Physical Society.]

The big advantage of this technique is the combination of a rather good time resolution of a laser with a very high and flexible probe energy of a synchrotron. The fact that the laser used for the femto slicing can also be used to generate the pump beam reduces jitter while the repetition rate can be about as high as the laser allows. Depending on the actual beamline, a disadvantage might be a low photon flux. The main disadvantage, however, clearly is the high complexity of such a setup, which leads to a rather limited accessibility.

3.1.4 Free-electron lasers

One can almost view a free-electron laser (FEL)[21] as a linear synchrotron. As a synchrotron it uses an electron beam and undulators to generate light. The difference is mainly in the longer undulator and the higher quality of the electron beam, which is achieved by a linear instead of a circular accelerator. These two conditions together lead to an interaction of the emitted photons with the electrons as they travel through the undulator. This results in a microbunching of the electron bunches which in turn causes the emitted radiation to be coherent and much more intense. To make the electrons in the FEL emit fully coherent photons, though, the FEL has to be seeded. An FEL can either be seeded by an external light source as a laser[22] or an HHG source, it might seed itself in a controlled way[23] or might seed itself by basically amplifying its own random noise (self-amplified spontaneous emission (SASE)). Although an FEL is a coherent light source the longitudinal coherence is not very good and only an external or controlled seeded operation allows for fully longitudinal coherent beams with goes along with even higher intensities and better energy resolution. As every FEL is different, also the range of accessible photon energies is different but spans from the microwaves to X-rays. This energy range might, however, be limited by seed-laser energies. As FELs are pulsed sources, they feature repetition rates which can also be very different. They are primarily dependent on the accelerator technology used where FELs with conventional technology feature repetition rates which are typically about 60 Hz to 120 Hz, while FELs with superconducting technology have repetition rates in the kHz up to tens of kHz.

The advantage of FELs lies in the short pulse length of coherent radiation at low wavelengths with extremely high peak powers in the order of 10^{10} W.[21] Pulse lengths are typically tens of femtoseconds, however, sub 1 fs second pulse lengths have been demonstrated.[21] This allows especially for single-shot coherent imaging techniques widely used in biology to determine the structure of biomolecules.[24,25] A drawback of FELs based on the SASE principle is their rather random pulse structure and jitter, which limits their time resolution in pump-probe experiments. Actively seeded FELs provide better pulse stability and energy resolution and might even allow optical synchronization of the FEL pulse with a pump laser pulse to limit the jitter

between them. However, actively seeded FELs are even more rare and complex. The main disadvantage of FELs, however, is their large size, complexity and high price, which severely limits their accessibility.

3.2 The principle of high harmonic generation

The main technique used in this thesis is high harmonic generation (HHG) from a driving laser. As already touched upon in Subsection 3.1.2, high harmonic photons[10,11] are generated by focusing a short and intense laser pulse into a noble gas, resulting in radiation with photon energies of odd multiples of the driving laser photon energy. This radiation will be referred to as high harmonics within this thesis. Most commonly titanium-sapphire lasers (Ti:sapphire lasers) with a center wavelength of about 800 nm are used for this as their technological advances currently make them the laser system of choice to generate pulses with mJ pulse energy at pulse lengths in the low tens of femtoseconds.

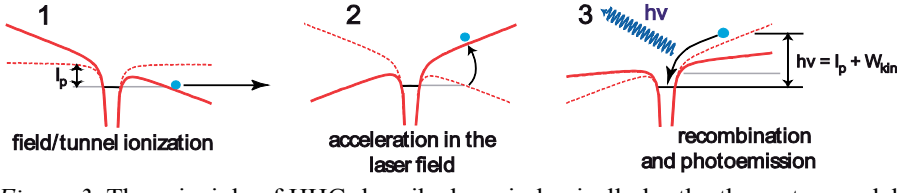

Figure 3. The principle of HHG described semi-classically by the three-step model. [Reprinted figure with permission from Ref. 10. Copyright 2016 by the American Physical Society.]

The process of HHG can be understood when split up in two successional processes. As a first step one has to understand what happens to a single atom when it is exposed to the strong electric field caused by the laser pulse. This can be explained in an intuitive way as described in *Figure 3* by the three-step model. (1) The electric field of the laser tilts the potential of the atom. This allows an electron to tunnel out of the atom, hence, (2) accelerating in the electric field of the laser. (3) When the laser field changes direction the electron is accelerated back towards the parent ion and can recombine with it. When recombining, a high harmonic photon with an energy equal to an odd multiple of the laser photon's energy is emitted.

As the electron can only gain a limited amount of energy within the laser field it is intuitively clear that there has to be a maximum high harmonic photon energy that can be generated this way. This energy is given by

$$E_{cutoff} = I_{pot} + 3.17\,U_p \approx I_{laser}\lambda_{laser}^{2}$$

where I_{pot} is the ionization potential of the atom and U_p is the ponderomotive energy of the electron in the laser field which is the average energy of an electron driven by an oscillating electric field of a laser with intensity I_{laser} and wavelength λ_{laser}.[11,26] This practically means that one has to use noble gases with higher ionization thresholds in order to increase the generated photon energies, although this proves to be less efficient at HELIOS. To simply change the laser wavelength is not possible as it is set by the used laser technology and could only be changed when exchanging the laser system. The intensity of the laser, however, cannot be chosen freely but needs to satisfy some other condition related to phase matching, explained below.

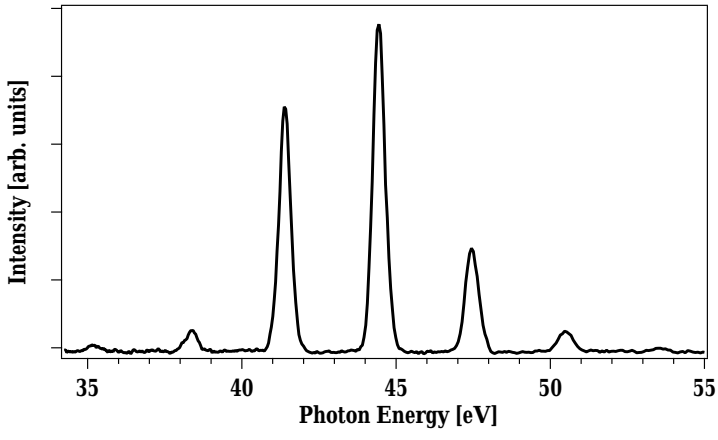

Figure 4. A typical high harmonic spectrum recorded at HELIOS by scanning the monochromator. The HHG process was optimized for the 29th harmonic at 44.5 eV. [Reprinted from Ref. 28 with the permission of AIP Publishing]

Apart from the response of the single atom to the intense laser field, phase matching is very important for the overall process of HHG as it is for the generation of harmonics in crystals in conventional laser physics. It is required that the laser radiation and the much higher-energetic high harmonics have the same phase velocity in the gas they travel in. Under this condition, all the emitted HHG radiation along the laser path interferes constructively and adds up to bright and coherent radiation. While the phase velocity for high harmonics in a gas is very close to the speed of light in vacuum, c, the phase velocity of the laser is slowed down by the gas to below c. On the other hand, the phase velocity of the laser can be increased by the presence

of free electrons in the gas. This allows matching the lasers phase velocity with the one of the HHG radiation by means of adjusting the gas pressure and laser intensity to control the degree of ionization in the gas.

The radiation created that way is temporally shorter than the driving laser pulse. Even lengths of tens of attoseconds can be reached.[10] However, the high harmonic radiation as used in this thesis, consists of a pulse train of sub-fs pulses. The length of this pulse train can be estimated by half the driving laser pulse length. The high harmonics maintain the polarization of the driving laser if it is linearly polarized. A circular polarized driving laser, however, results in no harmonics as the electron will not return to the atom from which it tunnel-ionized and, hence, cannot recombine. Nevertheless, it is possible to create circular polarized high harmonics if one overlays a circular polarized driving laser with its second harmonic, circularly polarized the opposite direction.[27]

The high harmonics generated within this thesis work are linearly polarized harmonics generated in a gas cell as described in Section 4.2. A typical spectrum of such harmonics is shown in *Figure 4*. However, beside gas cells there are also other ways of generating high harmonics, some of which are summarized in *Figure 5*. They all have in common that the gas volume is surrounded by vacuum since any air or even too long travel lengths of the high harmonics in the gas, in which they were generated, would lead to absorption of the harmonic radiation. The motivations for these different techniques are, in short, that a gas jet and a gas cell are rather simple solutions while a straight waveguide maximizes the interaction region of the laser and the gas by low-angle reflections of the laser in the waveguide while the waveguide additionally allows for high gas pressures. A modulated waveguide adds a modulated structure of the waveguide which modulates the laser intensity within the waveguide, allowing for quasi phase matching which significantly improves performance for high harmonics above 70 eV.[29]

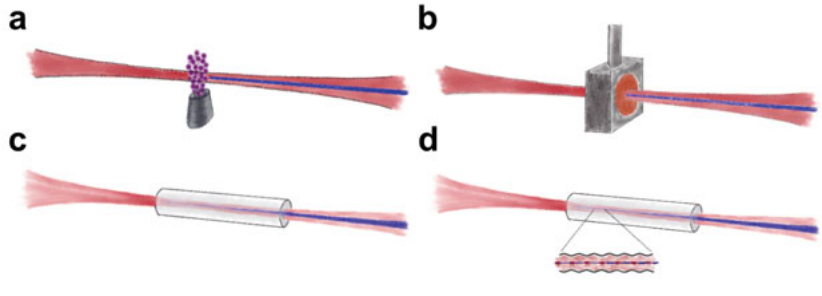

Figure 5. Different ways of generating high harmonics in a gas. (a) by focusing the diving laser into a gas jet, (b) a gas cell, (c) a waveguide and (d) a modulated waveguide. [Pictures taken from Ref. 30 with kind permission of the author.]

3.3 Properties of XUV radiation

The goal of high-harmonic generation as treated in this thesis is to create laser-like radiation in the XUV to be used for time-resolved spectroscopy. However, XUV radiation is rather difficult to work with for several reasons. Apart from multilayer mirrors, which basically only reflect a narrow wavelength region, there are no materials that would efficiently reflect XUV radiation in non-grazing incidence. Hence, achieving grazing angles onto optics in the XUV beam path is very important as shown in *Figure 6*.

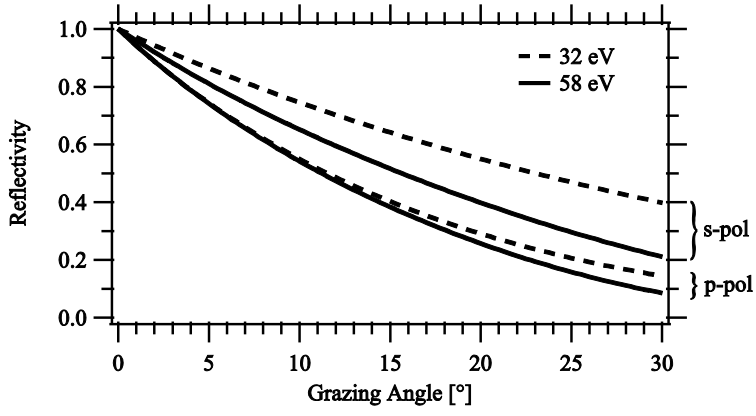

Figure 6. Reflectivity of a gold surface for different grazing angles. The reflectivity for s- and p-polarized light is plotted for 32 eV and 58 eV as these are the photon energies with the highest and lowest reflectivity within the energy range of 20 eV to 72 eV delivered by HELIOS.[31]

XUV radiation is also strongly absorbed by any material in the beam path. This needs to be considered when using filters, capping layers on samples or detectors with coatings. However, it can be necessary to transmit XUV radiation while blocking laser radiation, for example to separate the XUV radiation from the laser after it is produced in the gas cell or to separate the pump beam from the probe beam behind the sample. An aluminum foil can be used for this purpose as its transmission of XUV radiation is rather high and it can be produced as very thin foils. Nevertheless, even a 150 nm thick foil as used at HELIOS can absorb up to two thirds of the radiation. *Figure 7* shows the transmittance of such a foil and one coated with a 3 nm oxide layer on both sides, something almost impossible to avoid in practice. Additionally, the use of such a foil in the beam path particularly means that any radiation above the aluminum L-edge at about 72 eV is absorbed by the foil and cannot be used for experiments.

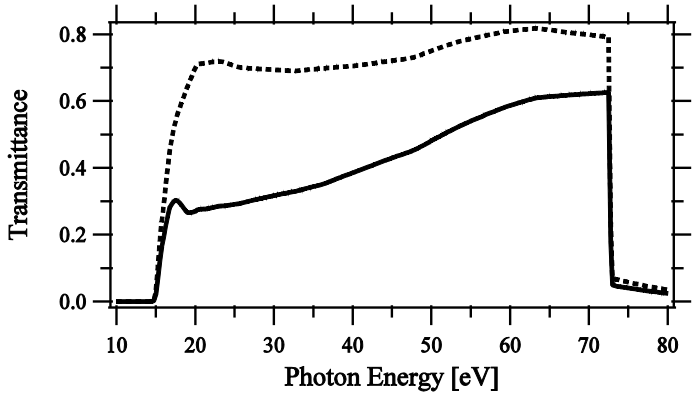

Figure 7. Photon transmittance through a 150 nm thick aluminum foil (dashed line) and though the same foil with 3 nm Al_2O_3 on each of its two surfaces (solid line).[32]

The probing depth of spectroscopy conducted with XUV radiation is very low. This is due to the very high absorption of XUV radiation in matter as already discussed, which allows only limited penetration depths, depending on the material. Even more relevant for electron spectroscopy, though, is the very limited mean free path of electrons with kinetic energies that correspond to XUV photon energies between 20 eV and 72 eV which are accessible at HELIOS. The mean free path of an electron is the average distance an electron could travel through a material without scattering and hence loosing energy or changing direction. This is typically discussed in terms of the

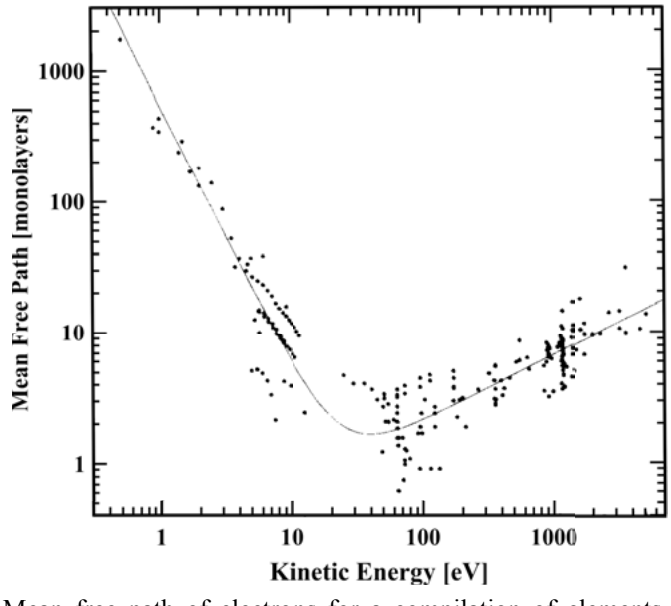

Figure 8. Mean free path of electrons for a compilation of elements. [Reprinted figure from Ref. 33 with permission of the copyright holder.]

universal curve, which is displayed in *Figure 8*. These two factors together make electron spectroscopy with XUV wavelength a very suitable tool to investigate surfaces.

An advantage of XUV radiation over conventional laser wavelength is that the photon energies are high enough to reach absorption edges of shallow core orbitals of nearly all elements. This enables time-resolved element-specific spectroscopy when using photon energies matching K-, L-, M-, N- or O absorption edges of elements in a sample. This is for example of importance when performing experiments employing the transverse magneto-optic Kerr effect (T-MOKE) as described in Subsection 6.6.1 and Paper V. Alternatively, ionizing electrons from weakly bound core levels can also enable time-resolved element-specific spectroscopy.

A higher photon energy above the visible or UV is also desirable for angle-resolved photoelectron spectroscopy. It allows probing a larger part of the k-space, assuming a fixed angular acceptance of a photoelectron analyzer. This becomes apparent in Section 6.4.

3.4 Monochromatization

When designing HELIOS one of the goals was to monochromatize the generated high harmonics, meaning that one should be able to select a single harmonic, or even only a part of a harmonic, to be used in experiments. This makes the whole lab flexible in how to perform experiments and makes its use similar to conducting experiments at synchrotrons or FELs. In general, a better monochromatization of the high harmonics means less spread energies within the XUV pulse which allows for better energy resolution at an experiment. However, selecting a smaller energy range also means reducing the photon flux.

Monochromatization of high harmonic radiation is typically done employing multilayer mirrors or diffraction gratings. The big difference between these two approaches is that multilayer mirrors only efficiently reflect photons in a narrow energy band, which means that the desired photon energy needs to be known when installing them and cannot be changed easily. If these restrictions are acceptable, monochromatization with multilayer mirrors offers high transmission.

A grating, however, diffracts all energies but in different directions which separates them spatially. This is described by the grating equation

$$\boldsymbol{d(\sin\theta_{in} - \sin\theta_{dm}) = m\lambda} \tag{1}$$

in which d is the distance of two adjacent grooves on the grating, θ_{in} is the incident angle meaning the angle between the grating's normal and the incident beam while θ_{dm} is the angle between the grating's normal and the direction of the diffraction maxima, m the order of diffraction and λ the wave-

length of the diffracted radiation (compare *Figure 9*).[34] The intensity of the diffracted radiation goes down as the order of diffraction increases while the path length difference between two adjacent grooves is always one wavelength (λ) times the diffraction order. To increase the intensity around a certain diffraction angle, one can use a grating surface with a saw tooth pattern, which features a so-called blaze angle as shown in *Figure 9*. By choosing the right blaze angle one can support diffraction around the angle in which light would also be reflected, if it hit a single blazed surface. However, as a grating is not a mirror and all observed light is purely diffracted, a reflected beam cannot be observed.

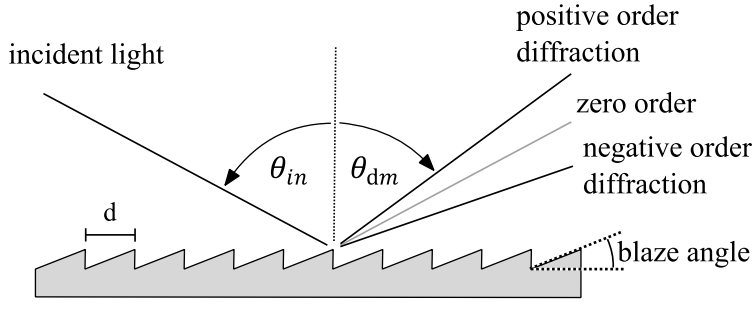

Figure 9. Schematic drawing of a blazed grating. [own work, published under CC0 license][35]

To monochromatize light with a grating, one normally uses a device called grating monochromator which allows the selection of one photon energy at a time and allows the change of this energy by simply rotating the grating. Up to a certain degree, it additionally allows to trade photon flux against energy resolution of the transmitted photons by changing the size of the monochromator exit slit.

There are various ways building monochromators. In HELIOS, the main focus was on simplicity, transmission and time resolution. In short, a parabolic mirror collimates the incoming light and reflects it onto a grating from which it is diffracted. By rotating the grating a certain center energy can be selected. This radiation is then focused by another parabolic mirror onto the exit slit of the monochromator which's opening can be changed to change the transmission and energy resolution. *Figure 10* shows a sketch of the monochromator.

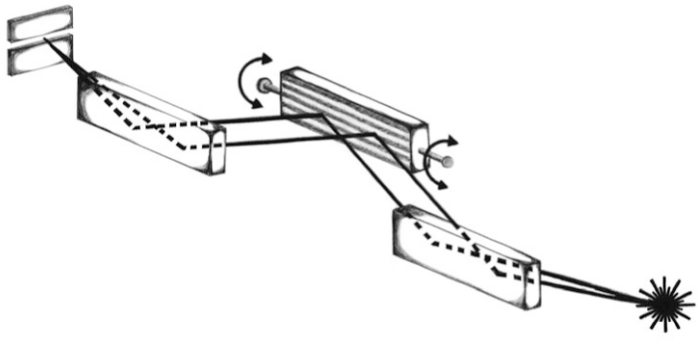

Figure 10. Schematic drawing of an off-plane-mount monochromator. The light from the source on the right diverges on a collimating mirror, hits a grating with the grooves along the incident direction of the light and is diffracted on a mirror that focuses on the exit slit. The rotation axis of the grating, used to select the transmitted energies is indicated. [Picture taken from Ref. 30 with kind permission of the author.]

As HELIOS is used for time-resolved experiments it is important that the monochromatized XUV radiation is not prolonged too much by the monochromator. However, diffraction from a grating is based on the existence of a path length difference between grooves. This means that a diffracted pulse in any order except zero will get more prolonged the more grooves are illuminated. More precisely, every single groove on the illuminated grating surface adds a path length difference to the diffracted radiation. The consequence of this is illustrated in *Figure 11* for a white light pulse. The path length difference adds up along the beam diameter so that the upper and lower edges of the beam feature different path lengths and the wavefront tilts. As the different wavelengths are diffracted in different angles according to equation (1) the beam additionally features an angular dispersion, which is in fact necessary to separate the different energies but also leads to special chirp.

One could use two gratings (one in positive, one in negative order), on the expense of a decreased transmission and higher monochromator complexity, to avoid an effect of the diffraction onto the pulse length.[36] At HELIOS, however, the grating is mounted in the so-called off-plane mount which means that the grooves are orientated along instead of perpendicular to the direction of the incident light.[37] This minimizes the amount of illuminated grooves and hence keeps the pulse prolongation at a necessary minimum while allowing high transmission and a simple design. Transmissions of above 30% have been demonstrated for such monochromators in the XUV.[38]

However, minimizing the number of illuminated groves also reduced the resolution of the monochromator. This is a disadvantage but acceptable,

because the maximum achievable energy resolution is in any way limited by the fact that a short pulse in time will have a broad frequency/energy spectrum.

To calculate the transmitted photon energies in the off-plane mount, the grating equation (1), needs to be expended by another angle as can be found in Ref. 38.

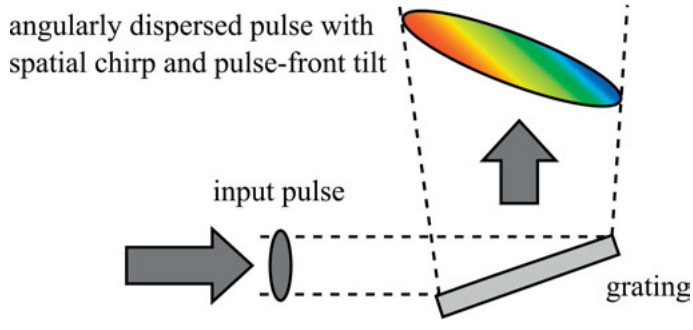

Figure 11. Diffraction of a short white light pulse on a grating, resulting in a tilted wavefront, angular dispersion and spatial chirp. [own work, published under CC0 license][39]

3.5 Fourier transform spectroscopy

A Fourier transform spectrometer (FTS) is used to measure the intensity of light depending on its wavelength. In that sense it is like a scanning monochromator where the transmitted light is recorded by a detector. However, the working principle and construction of such a spectrometer are quite different from a monochromator.[40,41] While a monochromator only allows radiation of a certain wavelength to be transmitted and detected by e.g. a photo diode, an FTS allows all radiation to be transmitted but instead introduces interference effects which result in a so-called interferogram which in turn can be converted into an intensity spectrum by means of a Fourier transform.

An FTS is an interferometer, like for example a Michelson interferometer as shown in *Figure 12*. It splits the photon beam and lets it travel two different paths before recombining the beam again and measuring its intensity. However, one of the two paths can be changed in length, which allows introducing and controlling an optical path difference (OPD) between these paths. This causes interference when the beams are recombined, which means that the intensity of the detected radiation is dependent on the OPD. Measuring this interference as a function of the OPD results in an interferogram. A Fourier transform of this interferogram then leads to the wavelength spectrum of the radiation (compare *Figure 12*).

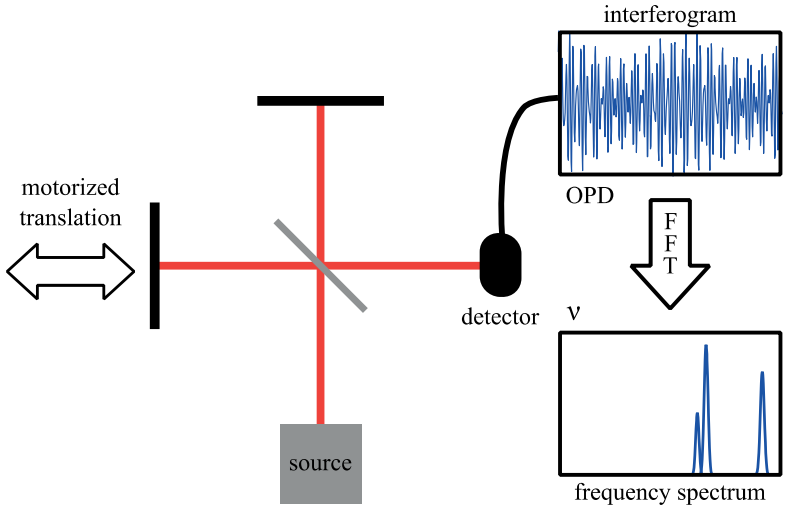

Figure 12. Schematic drawing of an FTS based on a Michelson interferometer. The frequency spectrum resembles the frequencies contained in the interferogram. [own work, published under CC0 license][42]

In the case of monochromatic radiation passing through the spectrometer, a change of the OPD by one wavelength alters the interference e.g. from constructive to destructive and back. In this case it is easy to understand that the Fourier transform of such an interferogram results in a spectrum with a single peak at the wavelength of the incident radiation. The same happens when multiple wavelengths enter the spectrometer simultaneously, only that different wavelength will have the interference maxima and minima at different OPDs. Hence, the resulting interferogram will look much less clear to the human eye. In any case, a Fourier transform of the interferogram will retrieve the wavelength spectrum of the incident radiation.

Fourier transform spectroscopy is widely used for the infrared and visible radiation due to their different and often superior signal-to-noise characteristic and high achievable spectrometer transmission.[43] In the VUV/XUV, however, the main advantages of an FTS over grating based spectrometers are the wavelength accuracy and potentially very high spectral resolution of an FTS.[41] The wavelength accuracy arises from the fact that the wavelength of the measured radiation can be determined by the spectrometer itself without the need of measuring a radiation source of similar energy and intensity for calibration purposes. The high resolving power R is given by

$$\boldsymbol{R = \frac{\lambda}{\Delta\lambda} = \frac{2L}{\lambda}}$$

where λ is the wavelength of the measured radiation and L is the OPD scanned during a measurement which means that the resolving power increases, with the scanning length.

However, utilizing these advantages gets more and more challenging as the wavelength decreases. One reason for this is that the requirements on the quality of the optics and the mechanical stability of the whole construction, as well as on the precision in setting and maintaining a certain OPD increase with decreasing wavelength. This is, because, the OPD has to be scanned in steps about four times smaller than the shortest wavelength to be detected, in order to achieve a clear interferogram. Additionally, the properties of VUV/XUV radiation discussed in Section 3.3 require the use of solely reflective optics in grazing incidence while keeping the number of reflections at a minimum in order to achieve a good spectrometer transmission. For the same reason it very challenging to produce beam splitters for this wavelength range. Additionally, an FTS in the VUV/XUV needs special detectors for this kind of radiation while the whole beam path needs to be kept under vacuum. Fulfilling all these requirements adds a lot of complexity to the spectrometers design. This, in addition to the characteristic of an FTS to be sensitive to detector noise, are probably the main reasons why FTSs are not widely used in these wavelength regions.[43]

4 HELIOS

The goal when designing HELIOS was to create an HHG-based facility for laser-pump XUV-probe experiments of various kinds, allowing for an overall time resolution below 50 fs. Possible samples span from well-defined surfaces in ultra-high vacuum (UHV), via organic molecules to liquids and gases. Accessible pump wavelength reach from 20,000 nm to 235 nm and probe energies from 20 eV to 72 eV are available. The design paper of the setup is Paper III and a CAD drawing of it can be found in *Figure 13*.

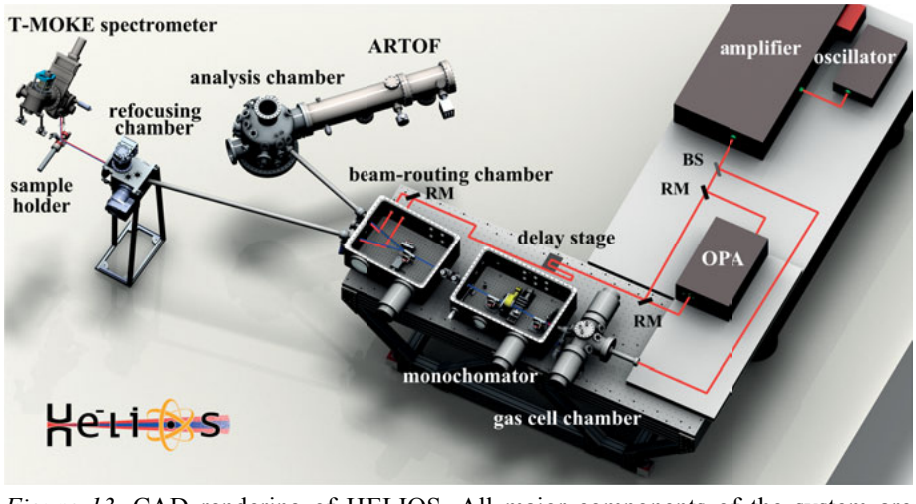

Figure 13. CAD rendering of HELIOS. All major components of the system are labeled. The laser beam path is only drawn schematically. The gray line labeled BS represents the beamsplitter while the black lines labeled RM represent removable mirrors. A schematic drawing of the beam path can be found in *Figure 17*.[44]

4.1 The laser system

The laser system at HELIOS is shown in the context of the lab in *Figure 13* and its technical specifications are listed in Table 1. It consists of an oscillator laser which generates ultrashort pulses with a very broad spectrum of wavelengths/frequencies. This is important, since the Fourier transform of a laser pulse in the frequency domain results in the pulse in the time domain. Due to that, only pulses with a broad frequency spectrum can be short in

Table 1. Specifications of the laser system, which's dimensions can be seen in *Figure 13*.

	oscillator	**amplifier**	
manufacturer	Coherent	Coherent	
model	Mantis™	Legend Elite™ Duo-USP-HP	
technology	passively mode-locked	stretched pulse amplification	
amplification medium	Ti:sapphire	Ti:sapphire	
repetition rate	80 MHz	5 kHz	10 kHz
center wavelength	806 nm	810 nm	
bandwidth	85 nm FWHM	46 nm FWHM	
pulse length	N/A	≤35 fs FWHM	
pulse energy	6.6 nJ	2.5 mJ	1.1 mJ
beam power	530 mW	12.5 W	10.5 W
polarization	horizontal	horizontal	
pump laser:			
repetition rate	constant wave	5 kHz	10 kHz
technology	optically-pumped semiconductor laser	diode-pumped intra-cavity doubled Q-switched Nd:YLF	
power	5.4 W	72 W	
wavelength	532 nm	527 nm	
pulse energy	-	14.4 mJ	7.2 mJ

time. As the oscillator laser only delivers very low intensity pulses, its output is amplified by an amplifier, which is described in the following subsections. The number of pulses delivered by HELIOS is determined by the amplifier and can be set to 5 kHz or 10 kHz.

4.1.1 Chirped pulse amplification scheme

The amplification of the oscillator pulses in the amplifier happens in a so-called chirped-pulse-amplification scheme. In short, the oscillator pulses first enter the stretcher, which features a grating to spatially separate the laser light. Thereafter, different wavelengths experience a different path length through the stretcher before they are recombined again. A schematic compressor/stretcher design is shown in *Figure 14*.

The resulting laser pulse is stretched in time by a factor of about 10,000 and spectrally ordered, which means that it is positively chirped since longer (redder) wavelength are in the front of the pulse while shorter (bluer) wavelength are in the back of it (compare *Figure 14*). This pulse stretching is applied as it allows amplifying the pulses while keeping the peak power in

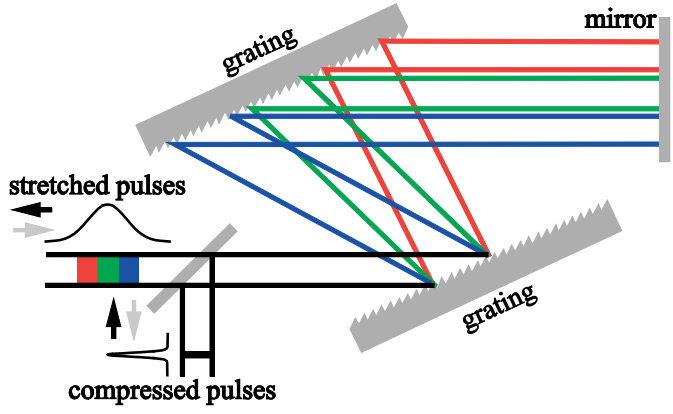

Figure 14. Schematic drawing of a stretcher. The compressed pulse from the oscillator laser enters from below and leaves positively chirped to the left, indicated by black arrows. Gray arrows indicate the use as a compressor for negatively chirped pulses. [own work based on image from Ref. 45]

the amplifier crystals and on optics rather low, which in turn prevents damages of optical components. After the amplification, the pulses are sent through a compressor, which is basically a reversed stretcher (compare *Figure 14*). The pulses get compressed so that they get short in time and have a high peak power when they leave the laser system.

4.1.2 Regenerative amplification

The amplification of the oscillator laser pulses happens in the amplifier after the pulses passed through the stretcher. A regenerative amplification stage (Regen) is used, which is basically a laser resonator containing a Titanium:sapphire (Ti:sapphire) crystal which is pumped by the pump laser. When the oscillator-laser pulses reach the Regen, they are successively reflected out without being further amplified. Only if a Pockels cell turns the polarization of one of the oscillator pulses, this pulse is not reflected out of the Regen but captured inside it. This means that it passes the pumped Ti:sapphire crystal over twenty times, thereby being amplified. Another Pockels cell then turns the polarization of the amplified pulse again so that it leaves the Regen. That way, the repetition rate of the oscillator is reduced to either 5 kHz or 10 kHz while the pulse energy is increased up to 1.5 mJ.

Another feature of the regenerative amplification is the fact that the Regen is a laser resonator which determines the direction of the amplified laser beam emitted from it. Hence, a change of the incoming beam from the oscillator laser might make the amplification process less efficient but does not change the alignment of the amplified beam which is a big advantage when it comes to stable measurement conditions. Behind the Regen follows a second amplification stage, where the pulses pass once through a single pass

amplifier which is another pumped Ti:sapphire crystal. That way, the pulse energy increases up to 3.3 mJ. The beam is then expanded and passes the compressor where it is compressed to about 35 fs and loses some energy so that the resulting pulse only features a maximum pulse energy of ≥2.5 mJ. Note that the pulse energies in the amplification process were given for 5 kHz operation.

4.1.3 Pulse shaping

The laser system at HELIOS also features a Fastlite Dazzler™ which is an acousto-optic programmable dispersive filter[46,47]. The Dazzler system was installed during the buildup of HELIOS to gain more control over the laser pulses. The motivation for that was that the compressor of the amplifier lacks a scale to read its position, which makes it impossible to go back to a previous setting. This means that it is possible to change the linear chirp (second-order spectral phase) of the laser pulses using the compressor but with limited control over its settings. The Dazzler however, allows using discrete, restorable settings to alter the spectral phase of the laser pulses as well as to change the spectral amplitude. It directly allows compensating for potential second-, third- and fourth-order spectral phase, ultimately allowing for better pulse compression.

The Dazzler can only be installed in front of the regenerative amplification of the oscillator pulses in the Regen. This is because the amplified pulses are much too intense and would damage the Dazzler. Additionally, the transmission efficiency of the Dazzler is about 30% which would be an unacceptable loss of laser power if used after pulse amplification. Positioning the Dazzler in front of the amplification process on the other hand means that the loss of pulse energy of the oscillator pulses can be compensated by a higher amplification in the Regen. However, it also means that one has to be very careful in what settings to apply to the Dazzler. Incorrect settings could lead to too narrow bandwidths during amplification, which would nullify the concept of chirped pulse amplification and could lead to laser intensities inside the Regen that risk damaging the amplification crystals.

The working principle of the Dazzler can be described in short as follows. The linearly polarized light from the oscillator laser enters the birefringent crystal in the Dazzler as an ordinary ray as shown in *Figure 15*. An acoustic wave generated by a piezoelectric transductor travels along the propagation direction of the light. As the light is much faster than this acoustic wave, the acoustic wave can be regarded as a fixed crystal modulation. The acoustic wave is built such that it locally only features one wavelength. Every wavelength of the laser pulse that should be transmitted through the Dazzler can find some position in the crystal where the acoustic wave is phase matched with it. At that place in the crystal, a part of the energy of that very

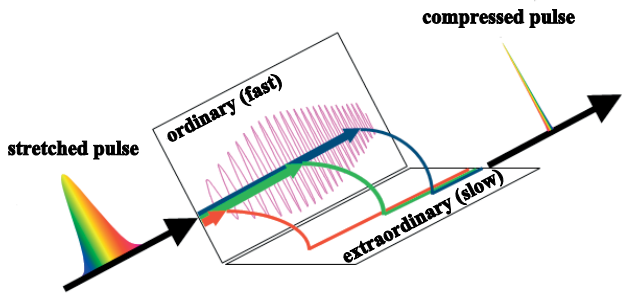

Figure 15. Sketch of the principle of operation of the Dazzler. In this example, a positively chirped pulse enters the Dazzler and leaves as a compressed pulse. The pulse enters the crystal as an ordinary ray and the different wavelengths are then successively diffracted, becoming a slower extraordinary ray. As the wavelength of the acoustic wave in the crystal (drawn in pink) is longer on the side where the pulse enters, redder wavelength are diffracted earlier and bluer wavelength can catch up. [Image published under Creative Common license][48]

wavelength from the ordinary ray is diffracted and becomes an extraordinary ray. By modulating the amplitude of the optical wave it is possible to shape the diffraction efficiency and hence the amplitude of the diffracted spectrum. As ordinary and extraordinary ray feature different phase velocities in the birefringent crystal it is also possible to shape the phase of the diffracted ray. This can be achieved as the position in the crystal at which a wavelength is diffracted determines the average phase velocity of the wavelength on its way through the crystal. Finally, the original (ordinary) and the diffracted (extraordinary) rays both leave the Dazzler with a slight angle which allows separating them spatially, which is used to amplify only the diffracted (shaped) pulse.

4.2 Probe-pulse generation

After the laser pulse left the amplifier it is first expanded and then sent to a beam splitter (compare *Figure 17* in Section 4.3). Different beam splitters are available and the used one should be chosen so that a laser pulse with at least 0.4 mJ is reflected. The reflected beam is then expanded again, passes an adjustment iris to manipulate its intensity and is thereafter focused into a vacuum chamber in which a gas cell is placed.

The positioning of the gas cell along the beam axis relative to the laser focus is possible by means of a linear piezoelectric translation stage, controllable from outside vacuum. The gas-cell entrance and exit consist of one 100 µm thick copper plate each, which can easily be replaced. This allows the laser to drill through these plates which makes the gas cell self-aligning. To achieve bigger holes and, hence, more laser intensity within the gas cell one

can substitute the copper plates by 40 µm thick titanium plates. This construction allows for gas pressures of above 1.2 bar in the gas cell, achieved with helium. In the early phase of HELIOS, a lens with a focal length larger than 500 mm was used to focus the laser into the gas cell. At the same time, there was no beam expansion by telescope 2 in front of the lens as displayed in *Figure 17*. It turned out that the aluminum foils in the monochromator could not stand the resulting laser intensities reliably, so that the lens was changed to a 500 mm focal-length lens while the beam diameter was enlarged. This made it necessary to reduce the length of the gas cell from originally 16 mm to 2 mm as this fits much better to the confocal parameter of the 500 mm focal-length lens currently used.[11]

All optics in the XUV beam path are gold coated and used in grazing incidence while the whole beam path is kept under vacuum. The grazing angles are displayed in *Figure 16*, which also displays the XUV beam path. After the laser enters the gas-cell chamber it generates XUV radiation in the gas cell. Thereafter, both the laser and the XUV radiation reach the monochromator which's general design is described in Section 3.4. A 150 nm to 200 nm thick aluminum foil reflects the laser radiation out of the beam path while the XUV radiation is transmitted, then collimated by a parabolic mirror and sent to the grating. A translation stage can be used to position different gratings in the beam path. The translation stage and, hence, the grating can then be rotated to select the energy to be transmitted. Three different gratings featuring different groove densities for different energy resolutions and different blaze angles for different energy ranges as well as one mirror for the transmission of the full spectrum are available. Their specifications can be found in the appendix of Paper III. The XUV radiation is then focused onto the exit slit by another parabolic mirror behind the grating. The exit slit consists of two razor blades mounted so that they leave a small gap between them, which can be changed steplessly by rotating their mount. A new design based on translating the razor blades is built and will be installed soon, promising a much better restorability of the slit opening.

Two parabolic mirrors on a translation stage in the beam-routing chamber behind the monochromator allow reflecting the XUV beam into one of the two beamlines which are described in Section 4.5 and 4.6. The monochromator and beam-routing chamber are built with transparent acrylic-glass lids, which allows monitoring all components while the chamber is under vacuum. This proved to be very advantageous in a day-to-day operation.

High harmonics were generated in the gas cell using argon, neon and helium. As a rule of thumb, harmonics produced from argon efficiently reach to about 48 eV while those produced from neon reach up to the absorption edge of the aluminum filter at 72 eV but are only less than 10% as strong as the ones from argon. Helium can be used instead of neon, which was done as neon was not available due to a collapse of its production.

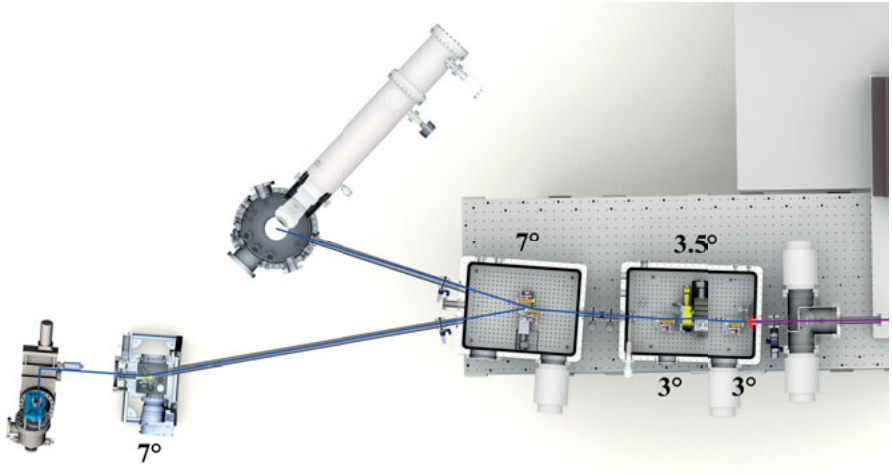

Figure 16. CAD rendering of the XUV beam path. XUV radiation is drawn in blue, 800 nm driving laser radiation is drawn in red. Grazing angles on the XUV optics are noted.[44]

It should be noted that the generation of high harmonics with neon or helium is much more challenging than with argon. The most reliable way of producing harmonics in neon or helium at HELIOS is to first produce harmonics in argon in order to optimize the phase of the laser pulse by means of the Dazzler. This is done by reducing the intensity of a certain harmonic from argon to below half its original intensity by means of decreasing the laser intensity with an iris. Thereafter one can optimize the Dazzler settings to retrieve as much intensity in this harmonics as possible. This procedure leads to a shorter pulse in the gas cell which compensates for the smaller initial pulse energy. These settings can then be used for the generation of harmonics with neon or helium directly, one can try to repeat the same procedure or repeat it with the actually desired gases.

4.3 Pump-pulse generation

The pump pulse consists of the laser pulse transmitted by the beam splitter (compare *Figure 17*). A Coherent OPerA Solo (sold by Coherent but built by Light Conversion) optical parametric amplifier (OPA)[7] can be used to convert this pulse to wavelengths between 235 nm and 20,000 nm. Different nonlinear processes are used inside the OPA to enable output in different wavelength ranges. This means that the output power and pulse characteristic can be rather different depending on the desired wavelength.

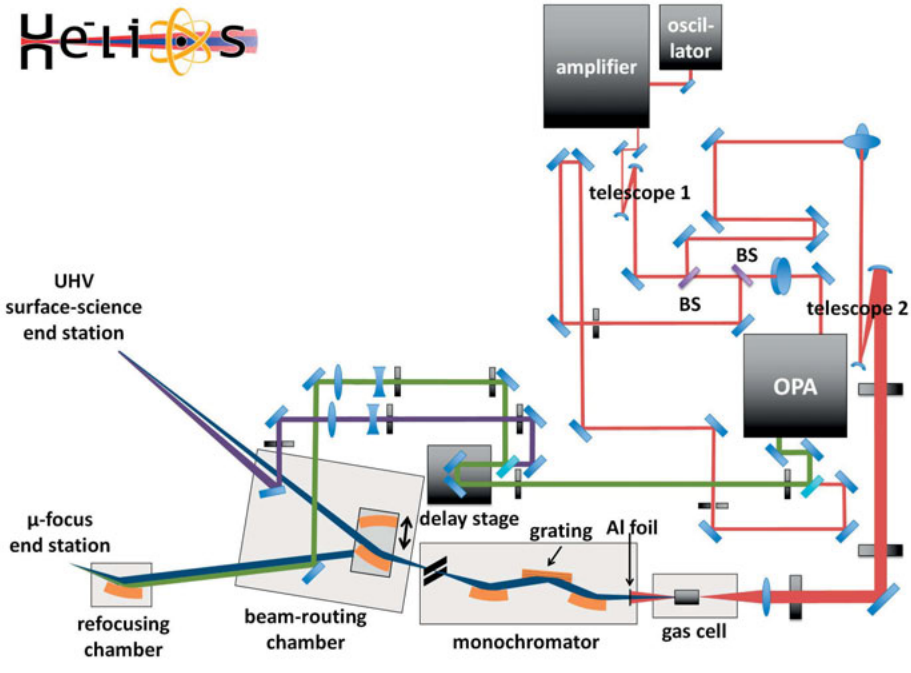

Figure 17. Schematic drawing of the beam path at HELIOS.

The output of the OPA is sent to a delay stage described in Section 4.4 and thereafter through a window into the beam-routing chamber from where it is sent towards one of the two beamlines. The beamline can be chosen by means of a flip mirror in the beam path behind the delay stage and a telescope in each beamline is available to manipulate the beam size of the pump beam on the sample.

Instead of the OPA radiation, one can also use the original 800 nm driving laser as a pump pulse. In that case the OPA is bypassed on a beam path with about the length of the inner-OPA beam path. The original driving laser beam can also be used to generate 400 nm in a frequency-doubling or 266 nm in a frequency-tripling process shortly before the beam-routing chamber. This promises an easier accessibility of lower pump wavelength with a higher photon flux compared to the OPA. Especially, as the beam path from the OPA to the sample features six to seven reflections more than the beam path from the doubler or tripler stage to the sample. The reflectivity for aluminum mirrors is quoted to be 93% which adds up to a theoretical value of about 35% to 40% extra losses. However, the actual reflectivities of these mirrors were found to be lower, leading to significantly higher losses.

4.4 Delay control

The delay between pump and probe pulse is generated by a relative path-length difference in the beam paths of the two beams. An Aerotech ANT130-160-L linear-motor driven linear-translation stage is used for this purpose, allowing a maximum delay of 1 ns (160 mm travel) and a bidirectional delay repeatability of 1.3 fs (±100 nm). It is placed in the pump beam path behind the OPA. Currently, two silver mirrors are mounted on the delay stage in a 90° angle as shown in *Figure 17*. This configuration can also be used for aluminum or dielectric mirrors, should this be needed to increase the beam intensity on the sample. The use of these mirrors, however, limits the maximum delay to some hundred ps as the delay stage tilts slightly in the vertical when moving. This tilting is within specifications and can be neglected when mounting a silver coated retroreflector, which is also available.

As already mentioned, the OPA can be bypassed on a beam path with about the same length as the inner OPA beam path while also the beam paths towards beamline 1 and 2 are about equally long facilitating changing the pump wavelength and beamline.

4.5 Beamline 1 – μ-focus beamline

As already displayed in e.g. *Figure 16*, HELIOS consists of two beamlines. A μ-focus beamline called beamline 1 and a UHV beamline called beamline 2. The μ-focus beamline is primarily designed for high vacuum and meant to be used for experiments on gases, liquids and particle beams, while slitless spectrometers also benefit from the small focal size. The XUV focus is designed to be well below 30 μm and a FWHM of 20 ± 3 μm has already been measured. However, it is primarily the flexibility in exchanging end stations, which distinguishes it from the UHV beamline. This combination of small focal size and flexibility was the main reason for using the μ-focus beamline for testing the liquid jet setup at HELIOS as described in Section 0. For the same reasons, this beamline is also very suited for measurements with the T-MOKE spectrometer described in Section 6.6.

The flexibility of beamline 1 has its origin in the design of the refocusing chamber, which is where possible end stations connect to HELIOS, as well as in the overall optical design of the beamline. The refocusing chamber can be positioned at any distance from the beam-routing chamber, which adds a lot of flexibility when mounting end stations. This is possible because the pump as well as the probe beam are collimated and travel collinearly towards the refocusing chamber. Both beams are then focused onto the sample by means of the same gold coated, parabolic mirror. The gold coating of the mirror, however, limits p-polarized (horizontally polarized) pump

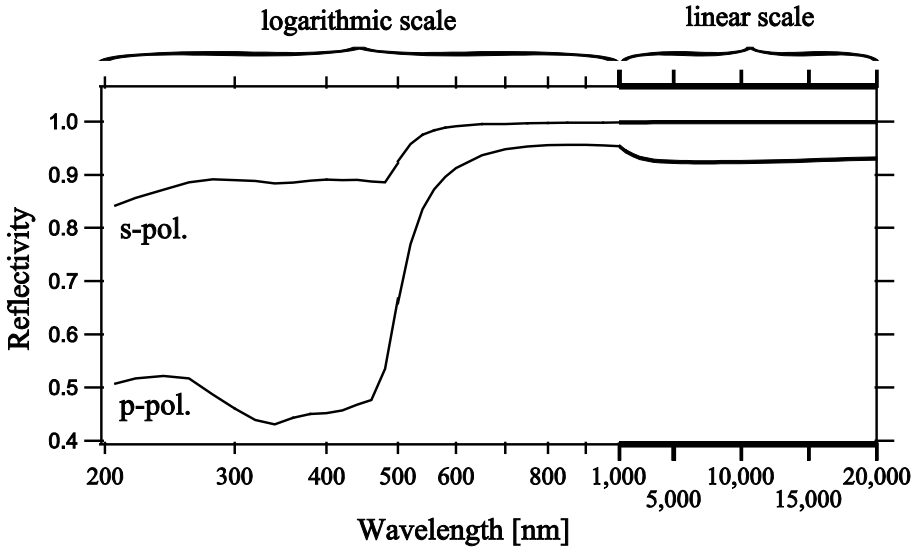

Figure 18. Reflectivity of s- and p-polarized light on a gold surface calculated for a grazing angle of 7° as for the refocusing mirror. Calculations employ data from Ref. 49 in the wavelength range from 200 nm to 500 nm and data from Ref. 50 in the wavelength range of 500 nm to 20,000 nm.

wavelengths to about 600 nm to 20,000 nm while s-polarized (vertically polarized) pump beams are practically not limited. The reflectivity of the mirror surface is shown in *Figure 18*.

The refocusing chamber itself has two main functions. It hosts the refocusing mirror and offers different flanges to connect to an end station (compare *Figure 19*). The mount for the refocusing mirror is placed on a flange so that it can easily been taken out together with all its connections. Two gold coated, parabolic mirrors with 400 mm and 600 mm focal length are available to be mounted. The refocusing mirror as well as all mirrors in the beam-routing chamber can be directed by means of piezoelectric motors from outside vacuum. The refocusing mirror can additionally be moved a total of 14 mm towards or away from the end station in order to allow positioning of the focus precisely onto the sample. When the mirror is moved to its center position, the distance from its middle to the flange surface, which connects to the end station, is only 186 mm. Within this distance, the refocusing chamber features a vacuum valve as well as a differential pumping stage. This allows using the chamber with end stations which feature higher pressures like e.g. a liquid jet setup.

The design of the refocusing chamber allows mounting it on any flange from DN 40 to DN 200 by just replacing the front flange with one of the appropriate size. Generally, the refocusing chamber can always maintain an upright position by matching the hole pattern of the front flange to that of the end station. In order to ease mounting of the refocusing chamber to an end

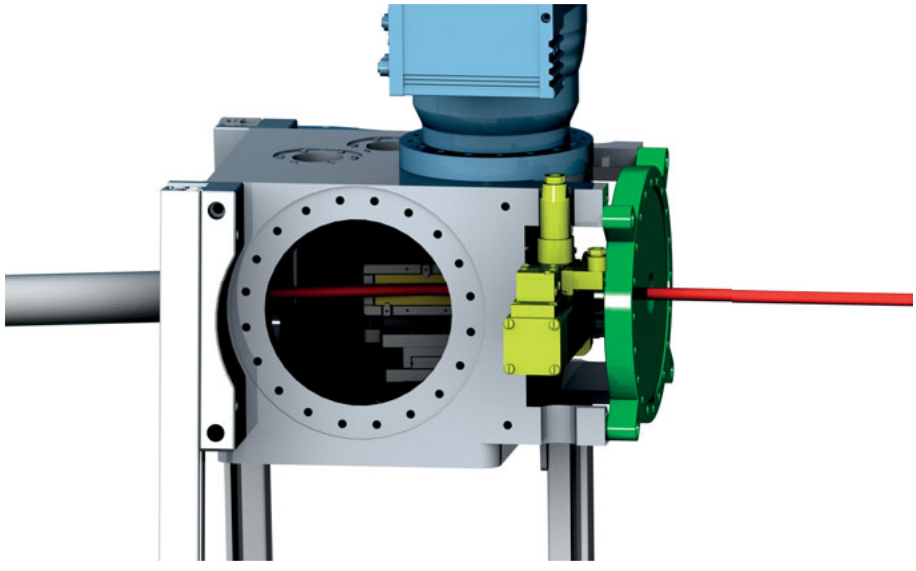

Figure 19. CAD rendering of the refocusing chamber. The radiation drawn in red enters from the left, reflects of the mirror surface and is focused outside this image to the right. Coloring marks two vacuum pumps in light blue (one hardly visible behind the chamber), a vacuum valve in yellow and the front flange to connect to an end station in green.[51]

station, the valve can be swapped to the other side. Additionally, the focal length of the refocusing mirror must match the distance from the mirror to the sample which might require additional spacer tubes to be mounted.

4.6 Beamline 2 – UHV beamline for angle-resolved photoemission spectroscopy (ARPES)

Beamline 2 at HELIOS is dedicated to electron spectroscopy in UHV conditions and, hence, also called UHV-beamline. The original plans envisioned that a Scienta SES100 hemispherical electron analyzer should be mounted semi-permanently at this beamline to be used for electron spectroscopy in high vacuum (HV) and ultra-high vacuum (UHV). This situation is also described in the design paper of HELIOS (Paper III). However, we had the possibility to perform tests using a Scienta ARTOF 10k (Angle-resolved time-of-flight)[52] spectrometer at this beamline which resulted in Paper IV. As these tests were very successful, it was decided to exchange the hemispherical electron analyzer at the UHV-beamline with an ARTOF 2 angle-resolved photoelectron spectrometer, which is a successor of the ARTOF 10K. The following description of the beamline will, hence, describe the beamline as it is currently built featuring an ARTOF 2 and a new analysis chamber as shown in *Figure 21* in Subsection 4.6.3.

The purpose of the UHV beamline is primarily to perform standard and angle-resolved photoelectron-spectroscopy experiments on solid samples under HV or UHV conditions. However, also a gas needle will be mounted to be used for gas-phase experiments as well as for the calibration of the temporal overlap of pump and probe pulse. A gold coated, parabolic mirror is mounted in the beam-routing chamber, focusing the XUV radiation from the monochromator directly into the UHV end station. The pump beam is focused outside vacuum by means of a telescope and then directed onto the sample by means of a plane, mirror in the beam-routing chamber. This mirror and the XUV mirror can be controlled from outside vacuum using piezoelectric motors. This design is rather simple and features a much larger XUV focus than at the μ-focus beamline, which is beneficial for electron spectroscopy as it reduces the risk of space charge on the sample surface.

4.6.1 Space charge

The risk for space-charge problems at HELIOS is much higher than at a synchrotron beamline although the average photon flux is typically lower. This is because HELIOS features a lower repetition rate and, hence, more photons per pulse than a synchrotron. Additionally, photo ionization at HELIOS happens within only a few tens of femtoseconds which leaves hardly any time for a charge transfer from the bulk of the sample to the surface, hence, leaving a charged area at the surface where the sample was hit by the XUV pulse. This charge then influences the emitted electrons which, hence, smear out in energy, and hinder spectroscopy. This is somewhat different from the typical effect of space charge at a synchrotron where space charge normally leads to an energy shift of the spectra instead of a smearing. The high acceptance angle of the ARTOF spectrometer counteracts space charge as it minimizes the photons per pulse needed to perform electron spectroscopy. This was one important consideration why to change from a hemispherical electron analyzer to an ARTOF spectrometer.

4.6.2 The ARTOF 2 angle-resolved photoelectron spectrometer

The ARTOF 2 electron spectrometer is an angle-resolved time-of-flight spectrometer. As all time-of-flight (TOF) spectrometers the ARTOF needs a pulsed photon source in order to achieve the same start time for all photoelectrons caused by one XUV pulse. Based on knowing this start time, the kinetic energy of the detected electrons is then calculated from their flight time. The main difference from non-angle-resolved TOF spectrometers is that the ARTOF allows the electrons to take different paths inside the spectrometer based on their kinetic energy and emittance angle. Non-angle-resolved TOFs try to prevent this as it leads to a smeared out arrival time of

electrons of the same kinetic energy, which would decrease their energy resolution.

The ARTOF, however, uses an electrostatic lens system that controls the flight path of the electrons through the spectrometer as shown in *Figure 20*. The lens voltages can be set so that the spectrometer has well defined and unique flight paths for electrons within a certain acceptance angle and a certain energy range around a center energy. The trajectories of these electrons can then be calculated which results in a so-called "lens table". This allows retrieving the initial kinetic energies and emission angles of the electrons from the measured flight times and detector positions. This retrieving does not work reliably for electrons outside the accepted emission angle and energy range, so that these electrons are neglected if they were not already discriminated by the lens system.[52]

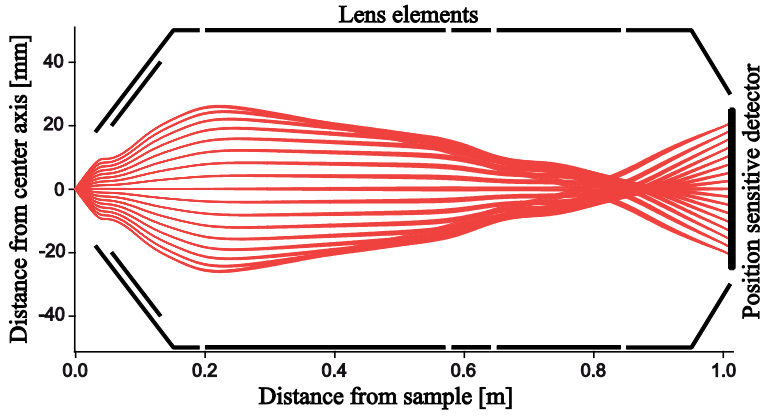

Figure 20. Schematic drawing of the lens system of the ARTOF illustrating the different paths of the electrons inside the spectrometer. The electron trajectories start at the left from a source with 0.2 mm diameter. The setting of the lens system allows measuring electrons with emittance angles up to ±15° relative to the ARTOF center axis. Trajectories are drawn for 10 eV kinetic energy and with a spacing of 2°. [Reprinted from Ref. 52, Copyright (2016), with permission from Elsevier]

The ARTOF 2 can achieve an energy resolution of 1.6 meV FWHM at 10 eV kinetic energy and an angular resolution of 0.06°.[53] However, these specifications are for a sample which is positioned in a limited volume in the focus of the ARTOF. The resolution will get worse if the illuminated sample reaches out of this volume, may it be because the XUV focal size is too big or the sample is tilted too much relative to the ARTOF. At least a degraded energy resolution is not a problem for experiments at HELIOS, though, as the spectrometer resolution is much better than the XUV energy resolution.

Due to the wide acceptance angle of the ARTOF 2 it is possible to measure all electrons emitted into a cone of 30° (measured from one side of the cone to the other) corresponding to a solid angle of $17/1000 \cdot 4\pi$ which is

two orders of magnitude larger than that of a traditional hemispherical analyzer.[52]

Being able to measure such a large part of the k-space simultaneously is a big advantage compared to an angle-resolved measurement with a hemispherical electron analyzer with which it would only be possible to measure a slit-like solid angle, which would only be a slice in k-space. To get more of the k-space, in the case of a hemispherical analyzer, one would then need to measure many times while rotating the sample. This would result in measured slices in k-space with unsurveyed volumes in between while drastically increasing the data acquisition time.

The large collection angle of the ARTOF also allows to measure with a low XUV intensity preventing space charge as discussed above. The fact that the ARTOF is a TOF results in a very good signal-to-noise ratio, which was not achievable with the Scienta SES100. This is, because a TOF only has a small time window in which e.g. dark counts could contribute to noise. All events detected at times not corresponding to reasonable electron energies are neglected. Such events would contribute to background in a hemispherical analyzer, though.

However, there are also disadvantages of the ARTOF. As it uses a microchannel plate on top of a position sensitive delay line detector, it can only reliably detect one electron per laser shot. This practically limits the detectable number of electrons to about 0.7 times the repetition rate of the laser, where this number is only a guide value and depending on the sample. The detector could in principle be upgraded to be able to detect five to eight electrons per shot using a so-called hexanode delay line detector but this would add significant extra cost. The high acceptance angle of the ARTOF requires a large opening of its lens system towards the sample, which means that the sensitive MPC is always under the risk of being hit by a reflected pump beam. A lot of attention has hence to be paid to prevent damaging the MCP. This big opening in line with the MCP detector also means that stray pump light could create counts in the detector system if the energy of the pump photons is high enough to eject electrons from the MCP surface. This was observed for 266 nm but not for 400 nm pump photons.

4.6.3 The experimental end station

The tests performed with the ARTOF 10k were conducted inside an old vacuum chamber which was available but did not fully satisfy the needs of pump-probe experiments. In parallel with purchasing the new ARTOF 2 a new UHV-compatible vacuum chamber is currently under construction and will be installed as an analysis chamber. It features an in-vacuum mu-metal layer to shield the inside of the chamber from external magnetic fields and is displayed in *Figure 21*. This chamber will have two different flanges

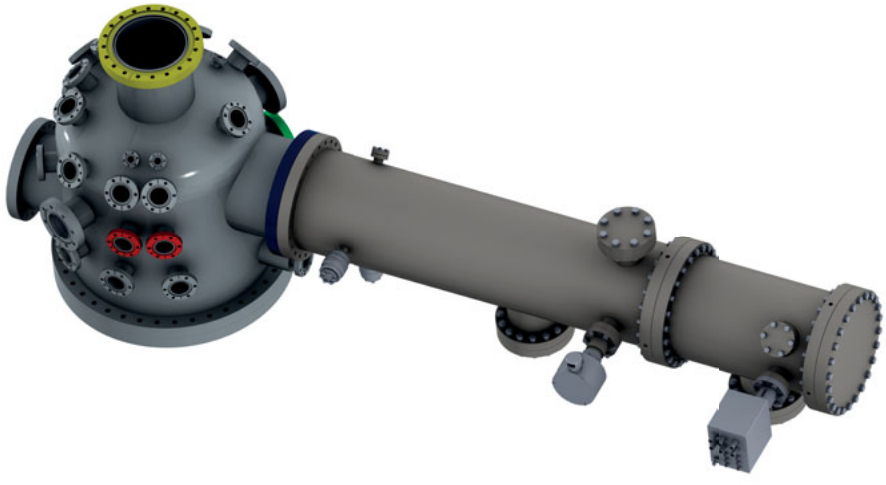

Figure 21. Rendering of the new analysis chamber and the ARTOF 2.[54]

(marked in red in *Figure 21*) to connect to HELIOS, one with a 65° angle relative to the ARTOF and one with 84°.

The analysis chamber will be equipped with a five-axis manipulator mounted on the top flange (marked in yellow in *Figure 21*) hosting a sample holder which can be cooled to 5 K by means of liquid helium. The manipulator will reach the height in the analysis chamber at which the HELIOS beams enter and the ARTOF is mounted (red and blue flanges in *Figure 21*). In addition to this height there is a lower level of the analysis camber, which will also be reached by the manipulator. This second level will host the sample transfer via a wobble stick to a transfer rod reaching in from the preparation chamber (connected on the partly covered green flange in *Figure 21*) as well as an evaporator to prepare samples. Additionally, the analysis chamber features a lot of flanges for viewports, a leak valve to let in gases, a gas needle for gas-phase experiments and a DN 160 CF flange on the bottom of the chamber which might potentially be used for molecular beams. Annealing the sample will also be possible but details are not yet decided on.

Attached to the analysis chamber will be a preparation chamber for sample preparation equipped with a load lock for the transfer of samples into vacuum, a mass spectrometer for monitoring the gas purity inside the chamber, a sputter gun to clean sample surfaces and a system to perform low-energy electron diffraction (LEED)[55] to investigate the surface structure of samples.

5 The Fourier transform spectrometer (FTS)

Beside HELIOS, which is without doubt the main project within my PhD thesis, testing the in-house-built Fourier transform spectrometer, very similar to the one described in detail in Ref. 6, was another project carried out at the synchrotron as well as at HELIOS. These two projects benefitted from each other more than once and resulted in a common publication, which is Paper II.

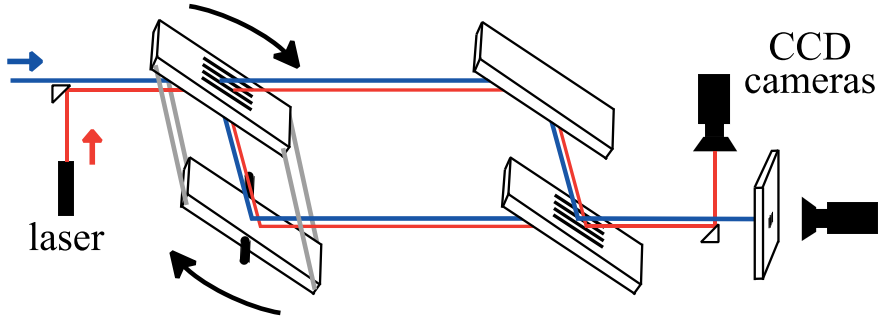

Figure 22. Schematic drawing of a Mach-Zehnder type interferometer as used in this thesis. The XUV light (drawn in blue) and the reference laser (drawn in red) enter from the left. The beams are split at the left and merged at the right to interfere on the detector. The left beamsplitter and mirror are mounted on an arm rotatable around an axis drawn in black.

The goal of developing this instrument was to push the wavelength limit for FTS further down into the XUV and to achieve a high acceptance to allow for emission spectroscopy. The design is based on a grazing incidence Mach-Zehnder interferometer as displayed in *Figure 22* using a wavefront-dividing beam splitter. The beam splitters are a key component for the function of the spectrometer. They are high quality mirrors which feature an area with a comb-like structure of alternating 100 µm wide slits and 100 µm broad mirror stripes as shown in *Figure 23*. These structures are both used as beam splitter and beam mixer where incident light is both reflected and transmitted. The optical path difference (OPD) inside the spectrometer is

controlled by the rotation of an arm by means of a Piezo stage. One beam splitter and one mirror are mounted on this arm. As a linear movement of the Piezo stage leads to a non-linear change of the OPD, a 650 nm diode laser is transmitted through the spectrometer in parallel to the XUV beam (compare *Figure 22*). The interference pattern of that laser is used as an optical ruler to measure the OPD for every Piezo stage setting.

Theoretically, it would be possible to focus the merged beams onto one spot and to measure its intensity for the interferogram to be Fourier transformed. Practically, though, the mirrors are not absolutely flat so that they introduce a spatial phase difference to the light, which would cancel a lot of the interference if focused to one spot. Hence, the beams are overlapped unfocused on a position sensitive MPC detector in front of a fluorescent screen, which is in turn recorded by a camera outside vacuum. An example of the resulting interference pattern is shown in *Figure 24*. Every pixel in this interference pattern is then Fourier transformed separately, nullifying the influence of different phases in different pixels.

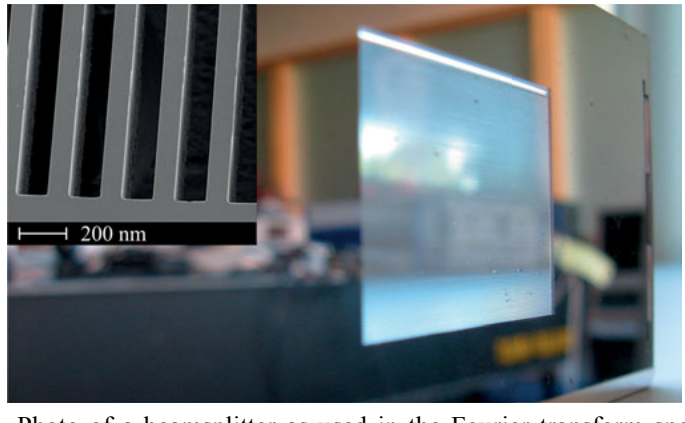

Figure 23. Photo of a beamsplitter as used in the Fourier transform spectrometer. The insert shows a scanning electron microscope picture of the reflective bars and slits, repeating with a period of about 200 µm.

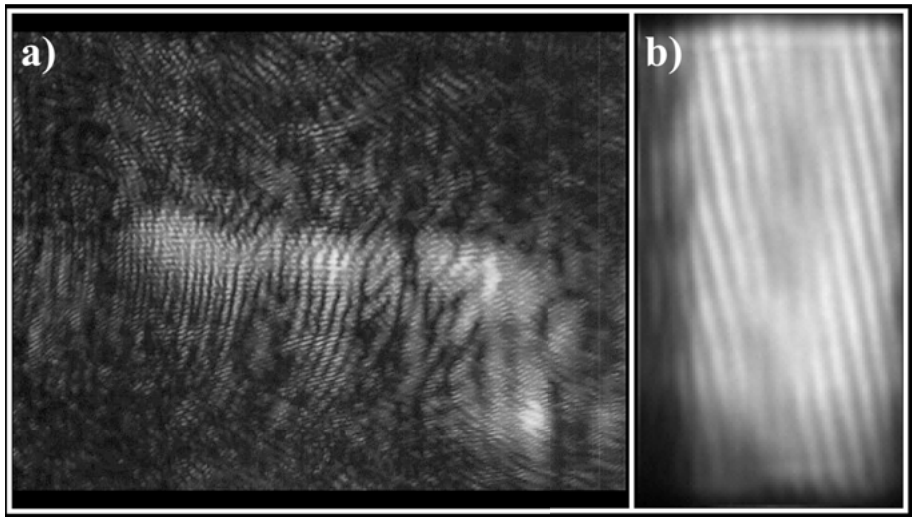

Figure 24. a) Interference pattern of the 650 nm reference laser passing through the Fourier transform spectrometer. b) Interference pattern of 25 eV XUV radiation from a synchrotron as used for Paper I. Note that the XUV interference pattern is enlarged by a factor of three relative to the laser pattern.

6 Experimental results

This chapter lists the milestones achieved within my thesis and puts them into context. They are listed in a chronological order except for the liquid jet experiments, which were actually performed at a rather early stage, between the temporal coherence measurements and writing the HELIOS design paper.

6.1 Concept test of the Fourier transform spectrometer

De Oliveira at al.[56] presented impressive results using an FTS with a resolving power of $1 \cdot 10^6$ down to wavelengths of 40 nm (31 eV). However, their design prevents much further reduction of the wavelengths as it features non-grazing reflections, which lead to a significantly weaker signal the shorter the wavelengths. In Paper I, we point out that it is possible to build wavefront-dividing beam splitters for the XUV (compare *Figure 23*). Employing these beam splitters enables a Mach-Zehnder-type FTS which's design also allows for detecting radiation with wavelengths shorter than 40 nm.

We demonstrate measurements of wavelengths from 124 nm (10 eV) to 22.5 nm (55 eV) with such an FTS as described in Chapter 5. These measurements were conducted at the beamline I3 at the MAX-lab synchrotron, Lund, Sweden.[57] The FTS was placed so that the focus of the beamline was 1 m in front of the spectrometer and the radiation diverging from it was directly passing through the FTS. The fact that no sample was used excluded all potentially disturbing influences of a rough and poorly reflecting sample surface. This setup, hence, allowed for the simplest test of the spectrometer with XUV radiation of tunable energy.

Figure 25 shows the spectra measured with the FTS at the synchrotron beamline. It is clear that the spectrometer is capable of determining the photon energy from 10 eV to 55 eV. However, it is also apparent that this determination is not very precise and that a lot of artifacts around the detected wavelength occur especially for the measurements above 30 eV. The reasons for this are numerous. The photon flux at the beamline decreased drastically

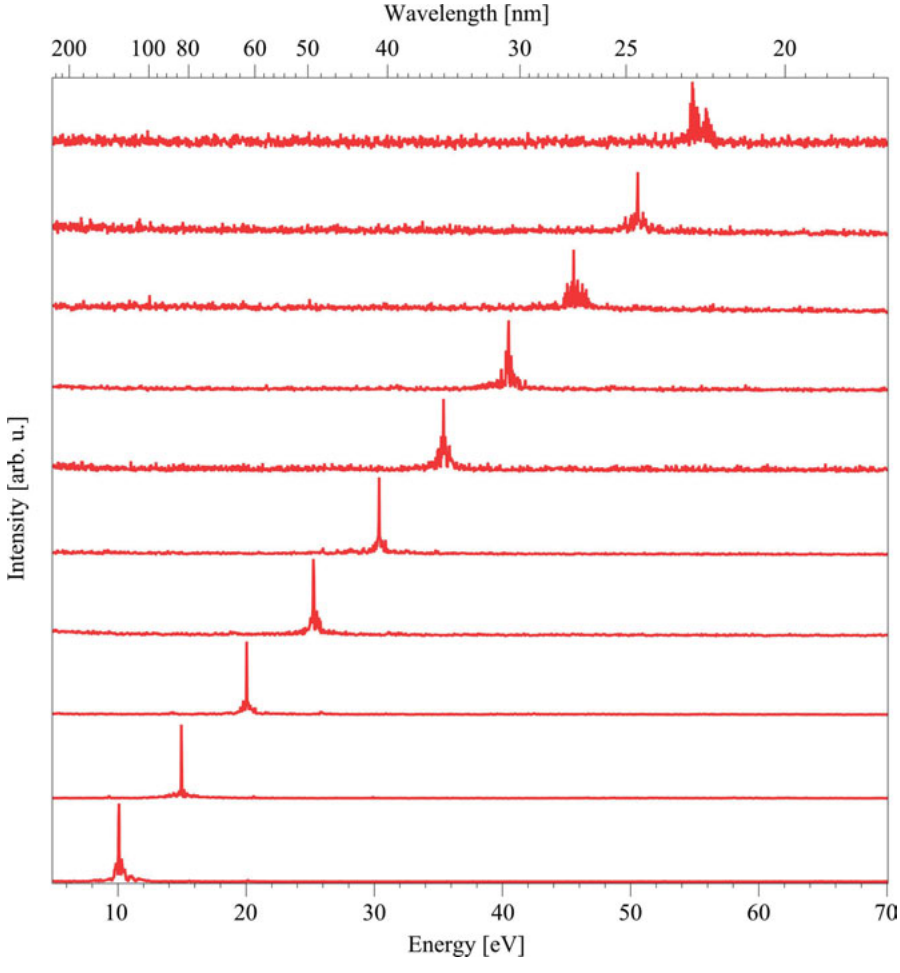

Figure 25. Spectra measured with the FTS at a beamline which delivered monochromatized radiation of tunable energy. [Reprinted figure from Ref. 58 with permission of the copyright holder.]

for energies above 30 eV. At the same time, the number of interference patterns recorded per OPD-change of one XUV wavelength decreases with shorter wavelengths. In parallel, the ratio between the XUV wavelengths of the detected radiation and the 650 nm diode laser wavelength, used to measure the OPD, gets worse with higher XUV energies. In addition to these wavelengths related factors, the unstable operation of the diode laser and the rather simple analysis software available at that time, further reduced the precision of the OPD measurement. All these factors together resulted in imprecise measurements of the OPD causing artifacts in the Fourier transform of the interferogram.

6.2 Measuring the temporal coherence of the high harmonics

By combining the FTS described in Chapter 5 and HELIOS in an early stage of its buildup process as shown in Figure 26, it was demonstrated that the FTS spectrometer is capable of measuring different wavelengths at the same time which could never be tested at the synchrotron before. However, interferences could only be observed as long as the path length difference in the spectrometer was smaller than the temporal coherence of the photons. This is actually a disadvantage for the spectrometer but meant that it was possible to extract the temporal coherence of the photons from the data of a normal FTS measurement. Not many measurements of temporal coherences of photon sources with photon energies above the UV were ever published, especially not with a rather mobile and flexible device as the FTS.

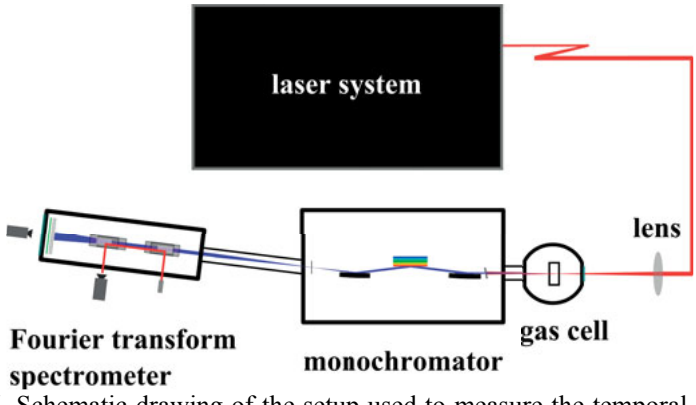

Figure 26. Schematic drawing of the setup used to measure the temporal coherence at HELIOS. The FTS was placed directly behind the monochromator. [Reprinted from Ref. 59, Copyright (2016), with permission from Elsevier.]

In Paper II we demonstrate the possibility of measuring the temporal coherence of an XUV photon source with an FTS, even with some spatial resolution. To obtain the temporal coherence, one needs to evaluate the OPD dependent visibility $V(OPD)$ of the interference fringes, which is

$$\boldsymbol{V(OPD) = \frac{I_{max}(OPD) - I_{min}(OPD)}{I_{max}(OPD) + I_{min}(OPD)}}$$

where $I_{max}(OPD)$ and $I_{min}(OPD)$ are the intensities of constructive and destructive interference for a small range of OPDs (compare *Figure 24* (b) for an interference image). The visibility of the interference fringes in a typical OPD scan is shown in *Figure 27*. From that, temporal coherence lengths of about 1.6 µm (5.5 fs), for high harmonics directly behind the monochromator, were obtained (compare Paper II for details). Please note that the

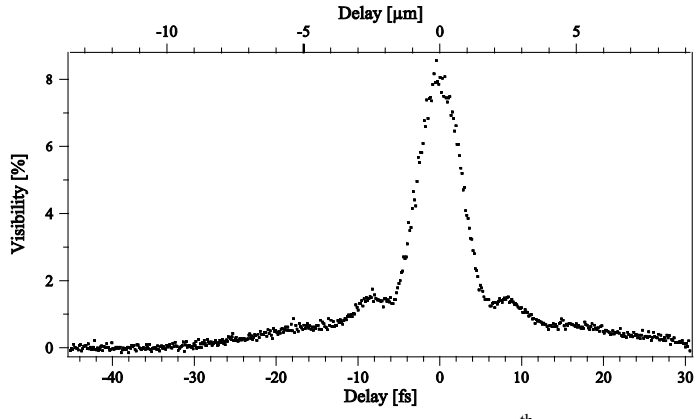

Figure 27. Visibility of the interference fringes of the 27th harmonic (42 eV) measured on the whole detector image. A constant background has been subtracted.

temporal coherence should not be confused with the pulse length. A second order process is required in order to measure pulse lengths and the FTS does not feature such a second order process but is based on a field autocorrelation.

6.3 Performance of HELIOS

The main work performed for my thesis was building, testing and improving HELIOS to a point where it was possible to use it for experiments. The fact that this was achieved is represented in the following chapters where it is demonstrated that both beamlines are operational and different kinds of experiments could be conducted at HELIOS. To set a solid base for future publications we wrote a design paper (Paper III) about HELIOS, which describes the design and characteristics of the laboratory.

For Paper III we determined the XUV photon flux behind the monochromator with a calibrated aluminum coated X-ray photo diode. As all data in this paper, the photon flux was determined with a laser repetition rate of 5 kHz. For harmonics generated in argon, we achieved $2 \cdot 10^{10}$ photons/second of the 29th harmonic at 44.5 eV with an energy resolution of 250 meV, using a gas pressure of 83 mbar. Alternatively we achieved $1 \cdot 10^{9}$ photons/second in the full 45th harmonic at 69 eV, generating high harmonics in 400 mbar of neon.

An essential part of determining the characteristics of HELIOS is to determine the XUV energy resolution and pulse lengths and how they are influenced by the monochromator settings. For that, we measured so-called sidebands as shown in *Figure 28*, which are basically a cross-correlation between the XUV pulse and the 800 nm driving laser. The sidebands were produced by focusing the laser and the XUV pulse into a helium gas jet so

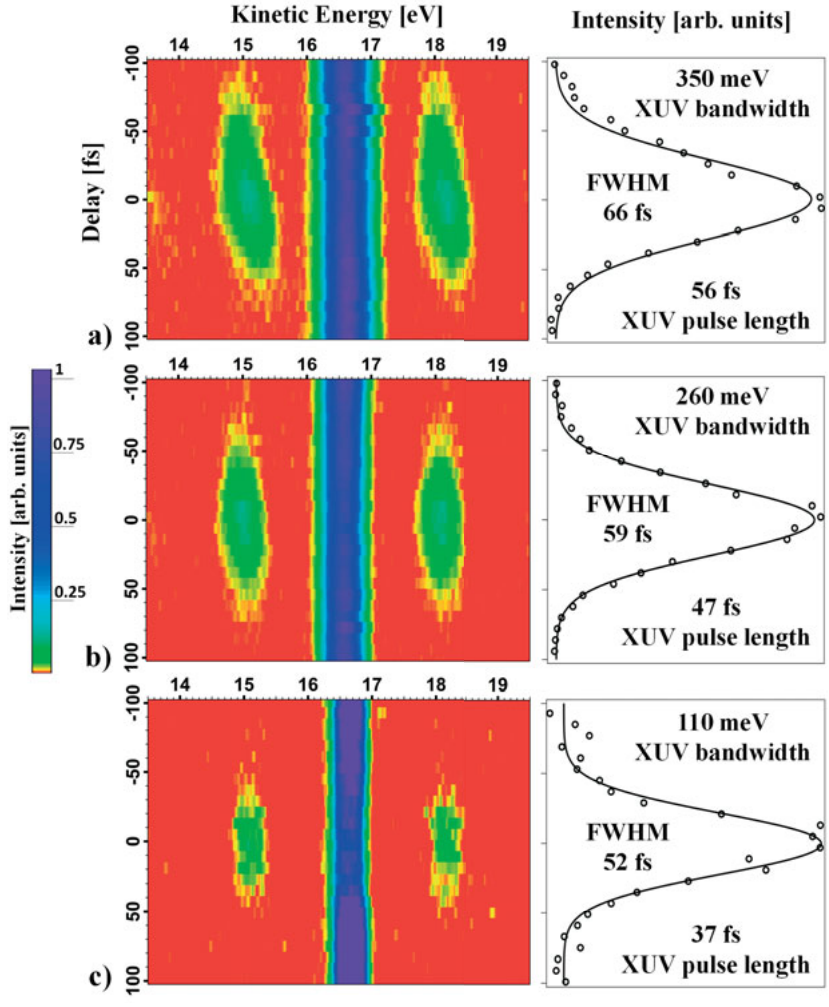

Figure 28. Left: Sidebands of He 1s from the 27th harmonic (41.4 eV) and 800 nm driving laser pulses measured for three different energy resolutions of the monochromator employing a grating with 500 lines/mm. Right: Corresponding temporal envelope of the sidebands with FWHM of the envelope. The energy resolution of the XUV radiation and the determined XUV pulse length are noted. [Reprinted from Ref. 28 with the permission of AIP Publishing]

that photoelectrons were emitted and measured by the Scienta SES100 hemispherical electron analyzer. A photoelectron in a sideband can have energies according to the XUV photon energy plus or minus the energy of one or several driving laser photons. However, sidebands can only be observed if both pulses overlap in the gas at exactly the same time. Measuring a sideband by changing the delay between XUV and driving laser pulse, hence, allows determining the XUV pulse length from the temporal width of a sideband. This is achieved by deconvoluting the sideband's temporal width with

the driving-laser pulse length, which, in turn can be measured easily by means of an optical autocorrelator.

Figure 28 displays sideband measurements conducted with different slit openings of the monochromator to observe the XUV pulse lengths for different energy resolutions. These measurements revealed that the XUV pulses actually got shorter when closing the monochromator exit slit for increased energy resolution, which might be an effect of a non-perfect monochromator alignment. It also demonstrates that 110 meV energy resolution at the 27^{th} harmonic at 41.4 eV photon energy can be achieved with an overall time resolution of 52 fs. We also showed that the XUV pulse length of the same harmonic in zero order diffraction is 17 fs while it is 23 fs for first order diffraction from the 120 lines/mm grating and 52 fs from the 500 lines/mm grating. This clearly shows the pulse prolongation due to the illumination of additional grooves.

It should be noted that the sideband measurements were conducted for 800 nm driving laser photons with a pulse length of 35 fs. Different pump wavelength might feature different pulse lengths which would, in turn, also alter the overall time resolution of HELIOS for these pump wavelengths.

In addition, Paper III demonstrates that HELIOS can be used for pump-probe measurements as it contains a photoelectron-spectroscopy measurement of a conducting polymer, which is described in detail in Section 6.5.

6.4 Angle-resolved photoelectron spectroscopy

By removing the hemispherical electron analyzer at the UHV-beamline used in Paper III, it was possible to install an ARTOF 10k (which is the predecessor of the ARTOF-2) at the UHV beamline for proof-of-principle experiments. The ARTOF 10k was only available for three months, hence, the goal was to test how the spectrometer would work in combination with an HHG source.

One concern that had been voiced was that the count rate achievable at HELIOS would not be high enough for an ARTOF to measure good data within reasonable time. The number of detected electrons is especially important as the ARTOF measures the emission angles as well as the kinetic energies of the emitted photoelectrons, which means that the detector counts distribute over three dimensions (two solid angles and one kinetic energy). The single hit characteristic of the detector in the ARTOF, however, reduced the maximum usable XUV intensity to a level where the ARTOF measures in average below one electron per laser shot. The laser repetition rates available were 5 kHz and 10 kHz, which is much lower than the repetition rates normally achieved at synchrotrons. BESSY II e.g. achieves a repetition rate

of 1.25 MHz in single bunch operation. This seems to result in a tremendous difference in count rate. However, a closer look reveals, that the radiation at a synchrotron also contains higher energetic photons of higher diffraction orders of the monochromator. They feature a multiple of the desired photon energy and, hence, cause a lot of additional counts in the spectrometer. In order to not overload the detector, the photon flux then has to be reduced to a level where the electron count rate in the desired energy window is typically at maximum 50 kHz which is much closer to the laser repetition rate.

It might be worth noting that HELIOS inherently features less of such problems with higher-diffraction-order photons as it is an HHG source. The reason for that is that the HHG process only delivers odd overtones of the driving laser frequency. The photon energy twice as large as transmitted by the monochromator in first order diffraction, which could be parasitically transmitted at the same grating angle in second order, is not produced in the HHG process as it would be an even harmonic. Additionally, HELIOS uses an aluminum foil that blocks radiation above 72 eV.

Time and Angle-resolved photoelectron spectroscopy of a graphene layer on a 6H-SiC(0001) substrate (Si terminated)[60] was performed in a pump-probe manner employing 800 nm as well as 400 nm pump pulses. The graphene layer was kept under UHV and annealed at 500° C for some minutes, while the measurement was performed at room temperature. An excerpt of a pump probe measurement on graphene, showing the Dirac cone of graphene at the $\overline{K}$ point is displayed in *Figure 29*. The data at the left shows a measurement taken at a negative delay of -1870 fs (before the pump pulse). A subtraction of this data set from a measurement at +50 fs delay is shown at the right. Both spectra were measured for 10 minutes at 10 kHz repetition rate with 42 eV photon energy.

Although the measurements were very successful, a detailed analysis of the recorded 4D data was delayed. The analysis will screen for more physics in the data than what is already known from previous "sliced" measurements with hemispherical analyzers.[61] However, we were already able to show that the measured angle-resolved data is of high quality and features a very high signal-to-noise ratio. Additionally, the data acquisition time for one spectrum turned out to be acceptable for pump-probe measurements. During these tries, no space-charge problems were observed and the spectrometer worked in the presence of an 800 nm and 400 nm pump beam.

It should be noted that especially angular resolved measurements benefit from the increased energy of high harmonics compared to standard laser energies. This increased energy allows a simultaneous probing of wider areas of $k_{\parallel}$. In the case of the Dirac cone of graphene, a photon energy of at least 16 eV is necessary to probe it,[61] meaning that this kind of measurements would not be possible employing laser-laser pump probe.

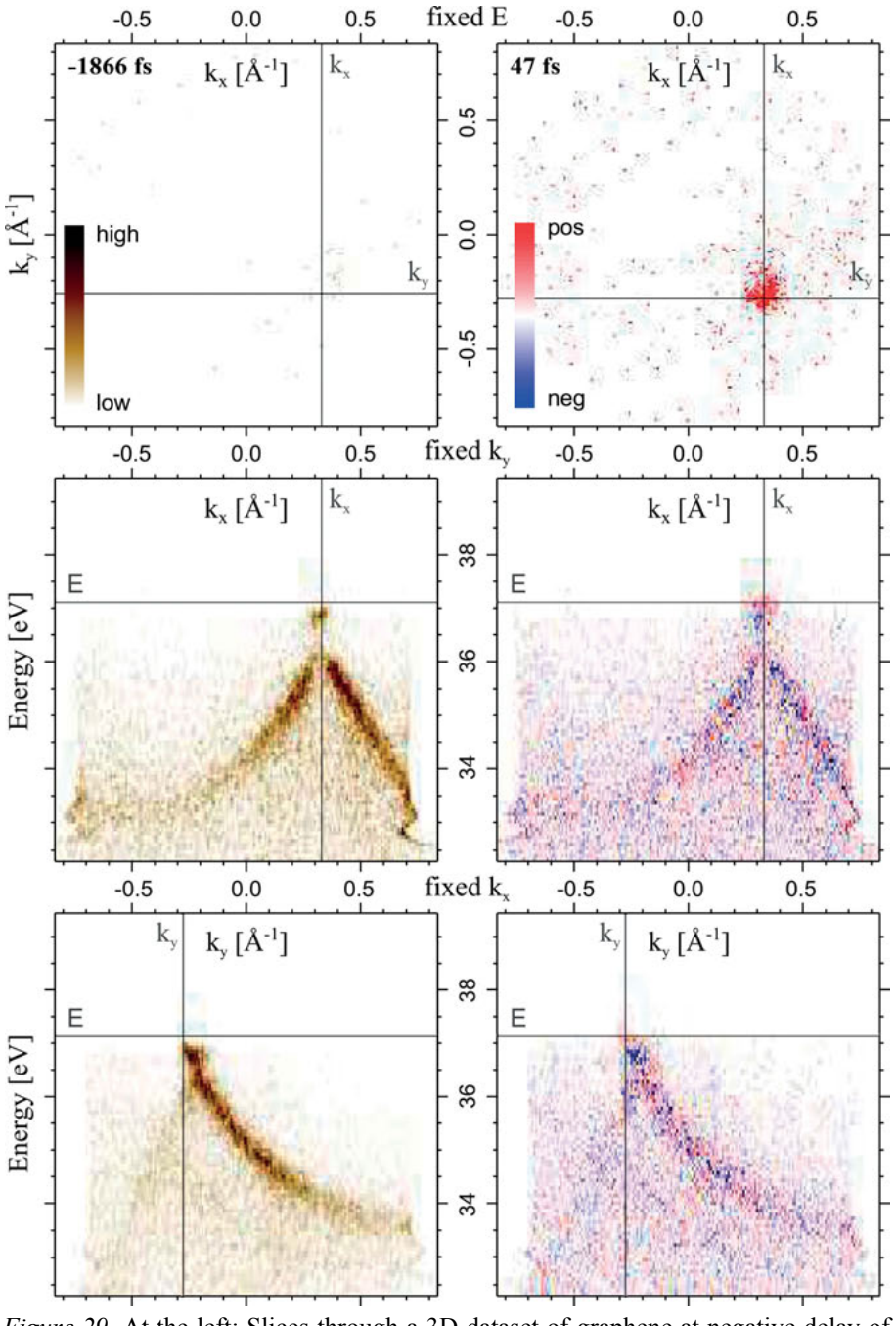

Figure 29. At the left: Slices through a 3D dataset of graphene at negative delay of -1866 fs (probe first). At the right: Difference dataset; left dataset at negative delay subtracted from a dataset at +47 fs delay. The slices feature a resolution of 71 meV and 0.0083 Å^{-1}. Gray lines indicate the position of the other displayed slices. Note that the color scale is different for every slice.

6.5 Photoelectron spectroscopy (PES)

The data from the ARTOF 10k can of course also be analyzed angle integrated, which then effectively makes it a "normal" photoelectron spectrometer. Samples related to organic solar-cell research were prepared in order to test the ARTOF's capabilities in a non-angle resolved measurement.

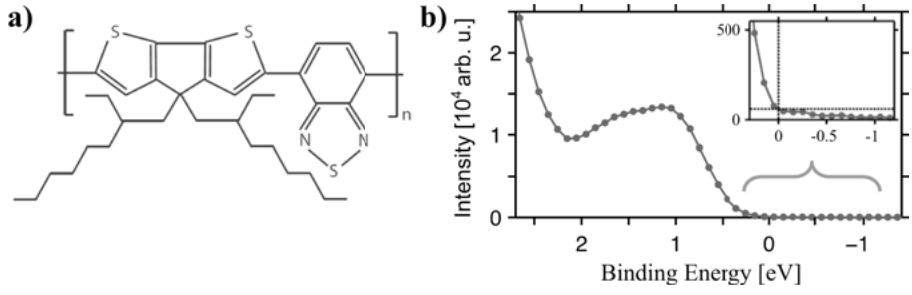

Figure 30. Molecular structure of PCPDTBT in a) and a valence photoelectron spectrum in b). Zero binding energy was set to the onset of occupied states, as shown in the inset. [Picture taken from Paper IV with kind permission of the author.]

Out of the prepared samples, time-resolved photoelectron-spectroscopy (TR-PES) measurements were conducted on a thin film of PCPDTBT[62–69] resulting in in Paper IV. PCPDTBT is a low-bandgap polymer and its molecular structure is displayed in *Figure 30* together with a photoelectron spectrum of its valence electrons. Pump-probe measurements were conducted with 800 nm as well as 400 nm pump and 39 eV probe radiation with a positive delay up to 4 ps (pump first). The pulse lengths of the 800 nm and 400 nm pump pulses were 35 fs and 110 fs FWHM respectively, while the XUV probe pulse had an expected pulse length of 38 fs FWHM (for more details see Paper IV). A clear excitation of the valence electrons could be observed for both pump wavelengths as displayed in *Figure 31* a) and b). More precisely, pumping with 800 nm (1.55 eV) photons allowed a detection of excited electrons up to about -1.2 eV binding energy, whereas pumping with 400 nm (3.1 eV) photons allowed a detection of excited electrons up to about -2.1 eV binding energy.

Figure 31 c) and d) display spectra measured at different delays. It is already apparent from these spectra that the excitation of the electronic structure mostly decays during the first 4 ps. A closer analysis of the transient behavior was carried out by introducing three different binding-energy regions (RgI, RgII, RgIII) as marked in *Figure 31*. The electron signal within each region was integrated for each delay position revealing that the electrons excited by the 400 nm pump pulse in RgIII decay rather fast with a decay constant of below 50 fs. The excitation in RgII, however, decays with a decay constant of about 1100 fs while electrons from RgIII seem to decay

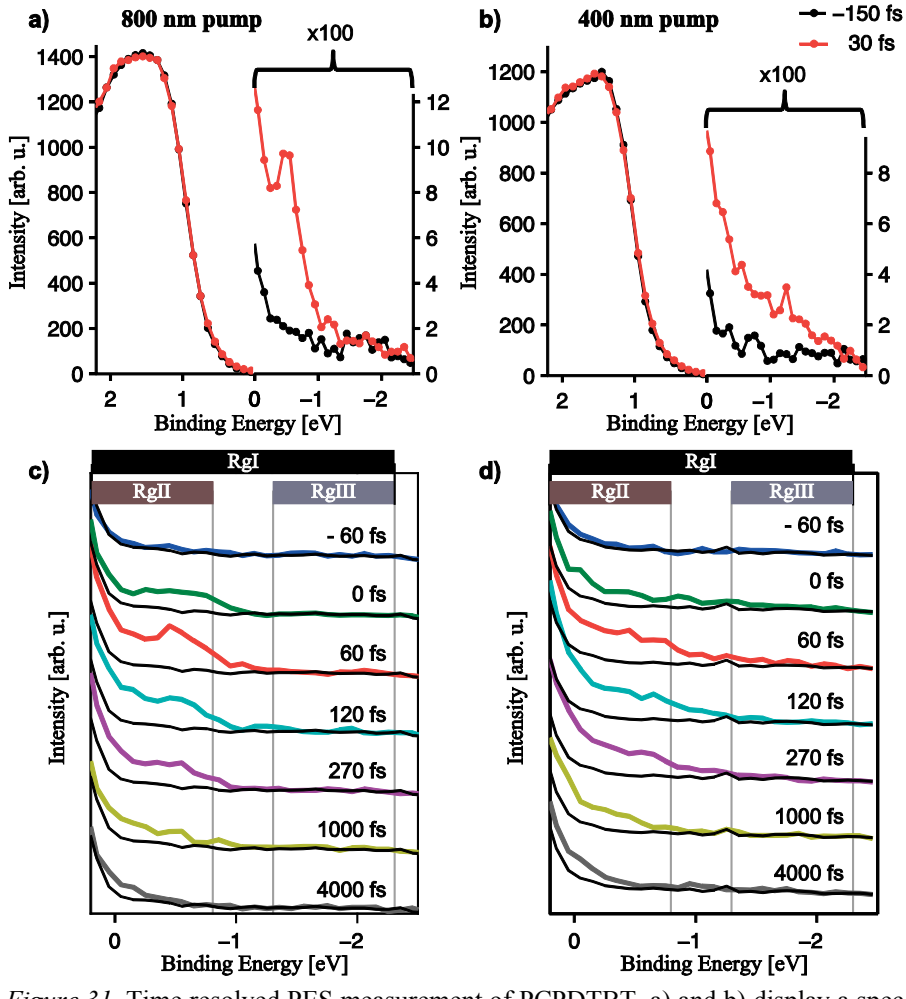

Figure 31. Time resolved PES measurement of PCPDTBT. a) and b) display a spectrum at 30 fs positive delay compared to an unpumped reference spectrum at negative delay. c) and d) display pumped spectra for different delays each in comparison to the same unpumped reference spectrum measured at -1000 fs negative delay. a) and c) were pumped with 800 nm radiation, b) and d) with 400 nm radiation. [Picture taken from Paper IV with kind permission of the author.]

into RgII shortly after the pump excitation. When pumped with 800 nm radiation, the decay constant for RgII is found to be 600 fs while no excitation could be observed in RIII. The overall excitation of electrons indicated by RgI, appears similar to the excitation into RgII, for both pump wavelengths.

The ARTOF 10k turned out to be also very well suited also for non-angle resolved measurements as it features a large acceptance angle, allowing measurements at low XUV photon flux where no space charge could be observed. The data acquisition time was acceptable for these kinds of measurements, although only up to one electron could be detected per laser shot,

due to the ARTOF's detector characteristic described in Subsection 4.6.2. More precisely, the data acquisition time per delay stage position was one minute, repeated eleven times to result in spectra as shown in *Figure 31*. The ARTOF's high signal-to-noise ratio turned out to be an important feature. This is because the weak signal from electrons which were excited by the pump beam would easily have been obscured by noise. The low signal level of the excited electrons compared to the neighboring valence-electron signal is apparent in *Figure 30* a) in comparison with *Figure 31* a) and b). This high signal-to-noise ratio is especially important, as the choice of PCPDTBT as a sample was motivated by the fact that it is a well-known polymer in solar cell research. Hence, it was not an option to increase the pump intensity until one would see the excited states emerging from a potential background. This is, since the dynamics in the polymer are only of relevance to solar cell research as long as one only excites a small fraction of the molecules in the sample at a time, as one would do in solar-cell applications. Additionally, too high pump intensities are likely to damage the sample.

6.6 Designing, constructing and commissioning the T-MOKE spectrometer

Employing the transverse magneto-optic Kerr effect (T-MOKE) allows measuring magnetization dynamics at HELIOS. Such measurements were performed by Mathias et al.[70] in a laser-pump XUV-probe HHG setup and allow for time-resolved element-specific measurements of the magnetization dynamics of thin films of magnetic materials.

6.6.1 Employing the T-MOKE effect

The basic idea behind these measurements is to place a sample in an external magnetic field which's direction can be reversed, hence, also reversing the magnetic field in the sample itself. The full spectrum of linearly-polarized high harmonics is generated without monochromatizing them and is reflected 90° off the sample surface as displayed in *Figure 32*. By measuring the change of reflectivity of the sample when reversing the magnetic field, one can calculate the so-called asymmetry which is related to the magnetic moment inside the material.[71] The asymmetry is given by

$$\boldsymbol{A}(\boldsymbol{\lambda}) = \frac{\boldsymbol{I}_{+}(\boldsymbol{\lambda}) - \boldsymbol{I}_{-}(\boldsymbol{\lambda})}{\boldsymbol{I}_{+}(\boldsymbol{\lambda}) + \boldsymbol{I}_{-}(\boldsymbol{\lambda})} \tag{2}$$

where $I_{+}(\lambda)$ and $I_{-}(\lambda)$ denote the intensity of the reflected radiation of wavelength λ for opposite directions of the magnetic field. A T-MOKE measurement requires that the polarization vector of the incident radiation is

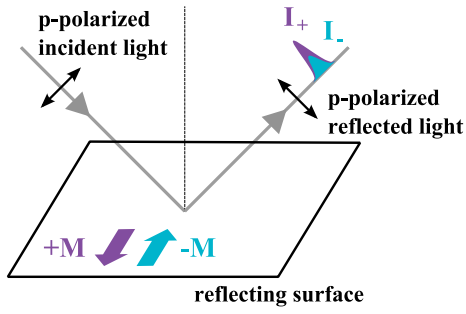

Figure 32. Diagram showing the geometry used for T-MOKE measurements. The change of reflectivity due to different orientation of the magnetization of the sample is indicated. [own work, published under CC0 license][72]

parallel to the plane of incidence (compare *Figure 32*). The asymmetry then probes the component of the magnetic moment perpendicular to the plane of incidence.

The asymmetry is most pronounced at the absorption edges of elements, which allows probing the magnetic moment with element specificity as e.g. the M-absorption edges have different energies in different elements (compare also *Figure 35*).

A simultaneous probing of the asymmetry at different absorption edges, hence, allows for a measurement of element-specific magnetization dynamics without relative temporal uncertainties, as they would be introduced by consecutive asymmetry measurements. A simultaneous probing thereby allows reaching a relative time resolution that is better than the time resolution of the cross-correlation of the pump-probe setup. In the case of HELIOS, this means that relative time resolutions of below 10 fs are achievable while the time resolution of HELIOS in an absolute asymmetry measurement would be above 40 fs.

To make use of this technique, one needs a way of simultaneously resolving and recording the intensity of different XUV energies of reflected HHG radiation. Mathias et al.[70] used an approach where they put a grating structure onto their sample, hence, making the sample itself a grating that disperses the HHG radiation onto an MCP detector. At HELOS however, we decided to build a spectrometer that can be placed behind almost any plane sample. That way one can avoid any potential interaction between the sample and the grating structure and simplifies sample production. Additionally, using a dedicated T-MOKE spectrometer led to an improvement in resolution compared to previously published results.[70,73–75]

6.6.2 Rowland spectrometer

A spectrometer, capable of separating the incident high harmonics without difficulty was deemed necessary. For that purpose, a slitless Rowland type spectrometer was constructed which is described in detail in Paper V.

A Rowland type spectrometer is a grating spectrometer which is designed so that the sample, the grating and the detector are positioned on a circle called the Rowland circle (see Ref. 76 and references therein).[77] The grating is not plane but has a cylindrical shape with a radius of curvature twice as large as the Rowland circle. The radiation emitted from the sample diverges onto the grating and is then diffracted and focused onto the Rowland circle as drawn in *Figure 33*. As the T-MOKE setup is placed at the μ-focus beamline, which tightly focuses the XUV radiation onto the sample, the spectrometer can be built slitlessly.

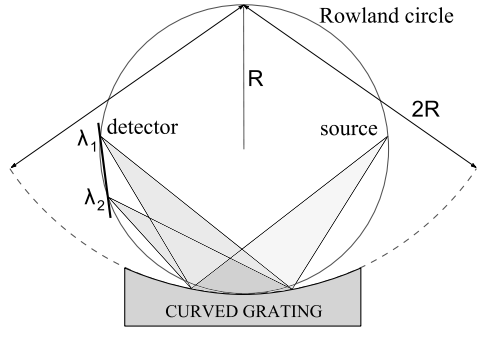

Figure 33. Schematic drawing of a Rowland spectrometer with a Rowland circle radius of R. [Drawing is based on a drawing from Ref. 78].

6.6.3 Spectrometer design

Apart from achieving a resolution which is sufficient to separate the high harmonics produced by HELIOS, the main focus of the development was on easy sample exchange and a robust operation. The spectrometer is meant to fit onto a MOKE vacuum chamber that was already available. This chamber features two in-vacuum water-cooled electromagnets on an iron yoke at which a newly designed sample holder was added. The spectrometer itself uses the same detector flange as the FTS described in Section 5 which features a chevron MPC in front of a fluorescent screen, filmed by a CCD camera outside vacuum. The delay stage of HELIOS, the electromagnets and camera are controlled by the same program allowing efficient and fast data acquisition. To avoid damages of the grating or detector, a 150 nm thick aluminum foil is placed in front of the grating to block the pump beam. A sketch of the spectrometer can be seen in *Figure 34*.

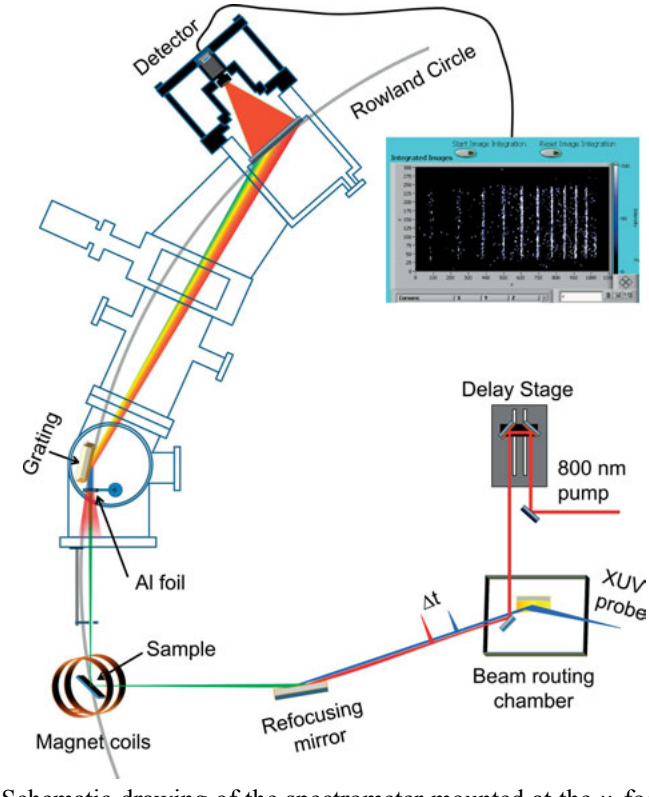

Figure 34. Schematic drawing of the spectrometer mounted at the μ-focus beamline of HELIOS. The inset displays a part of the data-acquisition program showing lines with different photon energies recorded by the camera. Image based on an image from Paper V. [Picture taken from Paper V with kind permission of the author.]

The spectrometer can disperse and measure all incoming energies within an energy window of 35 to 70 eV simultaneously. This allows performing measurements on all 3d transition metals (V, Cr, Mn, Fe, Co, Ni and Cu) as well as on many 4d transition metals.

6.6.4 Spectrometer performance and first results

By using the mirror in the monochromator instead of a grating, the full high harmonic spectrum can be transmitted. *Figure 35* a) shows such a typical spectrum reflected off a Permalloy ($Ni_{0.8}Fe_{0.2}$) sample for two opposite directions of magnetization, measured within about 3 seconds each. The high harmonics in the spectrum feature a width of about 400 meV FWHM, which is by far sufficient to resolve them. This width is primarily the energetic width of the high harmonics while the spectrometer resolution was determined to be about 170 meV at 42 eV photon energy.[78]

The overall spectrometer performance was tested by measuring the element-specific magnetization dynamic of a 10 nm thick Permalloy film,

capped by 2 nm of Ta to avoid oxidation. An 800 nm pump laser pulse with a pulse length of 35 fs FWHM was used to heat the electronic structure of the sample in order to demagnetize it, while a XUV pulse with an expected pulse length of 17 fs FWHM was used to probe the asymmetry. An extract of the recorded magnetization dynamic is displayed in *Figure 35* b). The whole delay scan took less than 48 hours and contains 75 pump-probe delays distributed over 500 ps. Details can be found in Paper V.

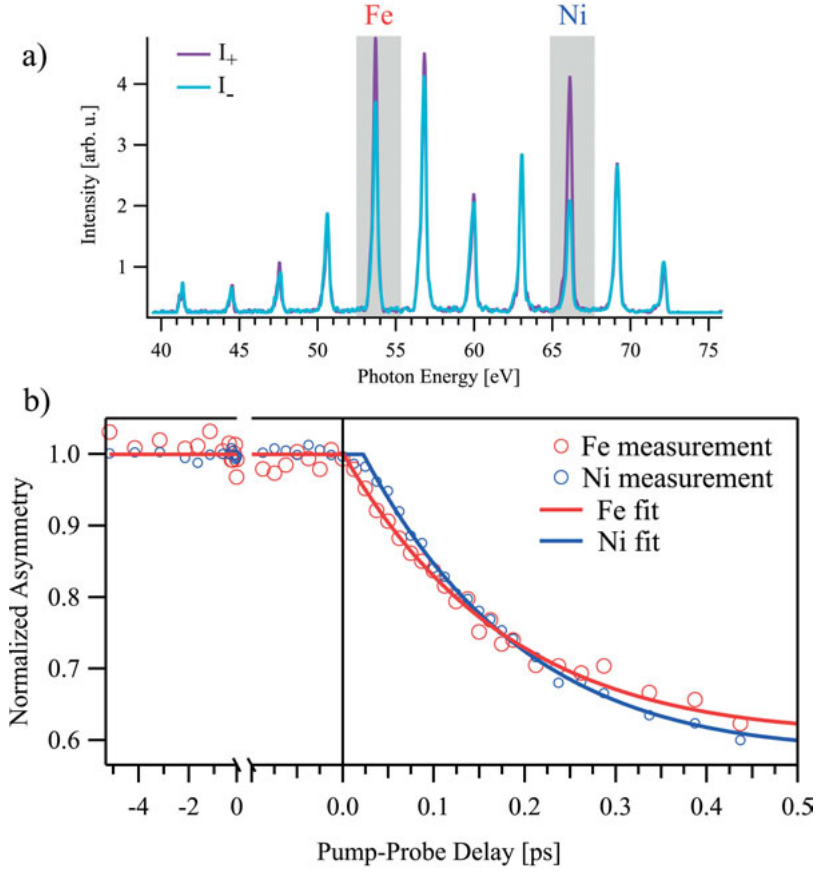

Figure 35. a) Recorded high harmonic spectrum reflected off a Permalloy sample. The large magnetization-dependent difference in reflectivity around the iron and nickel absorption edges is apparent. An asymmetry can be calculated from this data by means of equation (2). By averaging this asymmetry in each gray area, one obtains element-specific asymmetries. b) Element-specific asymmetries for iron and nickel plotted against the pump-probe delay. The asymmetries were normalized to 1, using values recorded at negative delays. [Picture taken from Paper V with kind permission of the author.]

When fitting the measured asymmetries with a triple-exponential function, it gets apparent that nickel demagnetizes 23±4 fs later than iron which is in agreement with Mathias et al.[70]. The demagnetization time constants for iron and nickel were measured to be nearly identical (Fe: 212±13 fs, Ni: 214.3±9.2 fs).

6.7 Liquid-jet experiments

Time-resolved photoelectron spectroscopy on liquids is potentially very interesting. We tested how to perform pump-probe measurements on liquids, using an existing liquid-jet setup, which has been regularly used at synchrotons.[79] A lot can be learned from these tries, although they were not very successful.

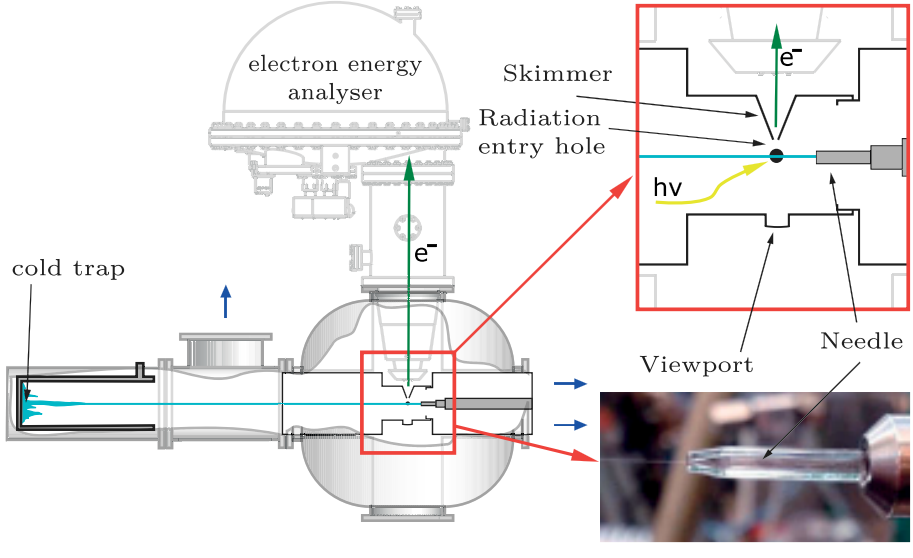

Figure 36. Schematic drawing of the liquid-jet setup. The insert shows the interaction region where the liquid jet is hit by the photon beam, which is coming in orthogonal to the plane of this drawing. Ejected electrons then leave through a skimmer into the electron spectrometer. A photo of the liquid jet shooting out of the needle is seen at the right. Blue arrows indicate pumping by vacuum pumps. [Image based on image from Ref. 80 with kind permission of the author.]

The liquid jet setup used employs a glass needle with a thin hole through which a liquid (normally water) is pressed into a vacuum chamber. The resulting jet has a diameter of 20 µm and is shown in a drawing of the setup in *Figure 36*. In order to preserve vacuum to allow electron spectroscopy on the liquid, the jet is shot in a cold trap, which is cooled by liquid nitrogen and is

installed opposite to the jet. Additionally turbomolecular vacuum pumps are used to maintain acceptable vacuum pressures. The liquid jet is contained in a tube inside the vacuum chamber. This is done to separate the poor vacuum around the liquid jet from the rest of the vacuum chamber and beamline, and especially from the electron spectrometer which requires high vacuum. The tube only features three small holes, two pinholes for the radiation of the light source to enter and exit the tube and one hole in a skimmer very close to the jet allowing emitted photoelectrons the leave the tube into the electron spectrometer. The geometry of the jet, the tube, the holes and the skimmer relative to the photon beam is illustrated in *Figure 36*. A Scienta SES 100 hemispherical electron analyzer is used as an electron spectrometer.

A general problem that is hard to avoid is that a 20 µm thick liquid jet in vacuum is a rather complex sample. The nozzle of the jet can clog or the liquid jet can freeze which requires venting its chamber to bring it back to operation. However, we faced more problems which made it impossible to perform pump-probe measurements on the jet but are generally avoidable if one knows about them.

Although proven to work at synchrotrons, a major problem was related to the liquid-jet setup, especially the tube around the jet itself. As HELIOS does not only feature one photon beam as at a synchrotron but a pump and a probe beam which come with a slight angle towards each other, the pinholes for the radiation were rather small. Additionally, the measurement of the photon flux inside the tube, which contains the jet, was not possible under vacuum. Hence, sufficiently large pinholes at the right places along the beam axis would have been necessary to transmit the beams through the tube. This would have allowed to determine whether the beams clip at the pinholes, as well as to determine the pump intensity in the interaction region by measuring the photon flux outside the tube. However, there was no way of positioning the radiation pinholes reliably and independently on the beam axis. Apart from that, the view onto the jet and the pinholes was rather limited and even the movement of the skimmer was coupled to the movement of the radiation pinholes. These shortcomings resulted in a situation where it was never clear whether the XUV beam is clipped, misses the jet or whether the spectrometer entrance is blocked by a malpositioned pinhole.

Beside these alignment issues, it turned out that an electron spectrometer based on the concept of a hemispherical analyzer as used for these trials, most likely features a too poor signal-to-noise ratio for this kind of experiment. It would have been necessary to detect a minority of pumped electrons energetically close to a vast majority of electrons in the ground state. However, the noise level in our spectra was about as high if not higher than what we would have expected as a signal from pumped electrons, making such time consuming and complex measurements rather pointless.

If one wants to perform pump-probe measurement on liquids, the issues described above have to be solved by completely redesigning the liquid jet chamber. An electron spectrometer with much better signal-to-noise ratio has to be used. This probably means to use a time of flight electron spectrometer instead of a hemispherical one.

Additionally, one should rethink the overall geometry of the setup. Photoelectrons will only be ejected on the illuminated side of the liquid jet, since XUV radiation below 72 eV, as available at HELIOS, only has an attenuation length of below 100 nm in water.[32] Photoelectrons with such low energies have a mean free path corresponding to only few monolayers, as discussed in Chapter 3.3. It would, hence, be beneficial for the observable count rate to place the spectrometer on the side of the liquid jet where the XUV radiation hits it.

A positioning of the spectrometer on the XUV-beam axis would also be beneficial for the controllability of the pump intensity on the jet surface. This is because the regions of the liquid jet with a surface perpendicular to the pump-beam propagation direction are observable in such spectrometer geometry. In contrast to that, the liquid jet setup, as it is now, observes the part of the jet, where the pump beam hits the jet rather grazing, so that the pump intensities on the jet surface are rather variable, if not unknown. Alternatively, one could use a flat liquid jet, which would add additional cost and complexity.

In the current setup, however, the spectrometer is placed in the magic angle[81–83] of 54.7° relative to the XUV-photon polarization and perpendicular to the beam propagation direction (the first is not apparent from *Figure 36*). That way, the influences of electron-emission anisotropies on the measured photoelectron signal are minimized due to the positioning of the spectrometer in the magic angel. Parallel to that, the signal from dipole emission relative to the influence of quadrupole emission is increased due to the positioning of the spectrometer perpendicular to the XUV propagation direction.

A new geometry of the setup has to be chosen carefully taking all these considerations into account, while aiming for fast and reliable data acquisition as well as for easy and reliable data analysis.

7 Outlook

While writing this thesis, the µ-focus beamline at HELIOS is operational and taking data using the T-MOKE spectrometer described in Section 6.6. The new analysis chamber for the UHV beamline is currently being built in the workshop. In parallel, the characteristics of an ARTOF 2, as it will be installed at the analysis chamber, are tested and evaluated in comparison to the ARTOF 10k which was used for photoelectron spectroscopy as presented in Section 6.4 and 6.5. To do so, the Scienta SES100 hemispherical electron analyzer which was used at the UHV beamline for the HELIOS design paper (Paper III) was moved into a separate lab. It will become an independent system for UHV sample preparation and analysis. In the long run, it is envisioned that sample transfer under UHV conditions from this system to HELIOS or vice versa will be possible, using a vacuum suitcase. That way, it will be possible to characterize samples before and/or after a pump-probe measurement by means of electron spectroscopy with x-rays from an x-ray anode or UV light from a UV lamp.

Although HELIOS is operational, there are a number of improvements which still need to be implemented in a short term. A new exit slit for the monochromator is built and needs to be installed to improve the restorability of the slit setting, as well as to ease the alignment of the XUV beam path. An automated system, allowing a stabilization of the pointing and positioning of the laser output was purchased. It was not installation yet, but is planned for the short term, leading to a new layout of the first halves of the beam paths. This upgrade is meant to ease the day-to-day operation of HELIOS, making it more time efficient and, thereby, meant to free time for other lab activities. The XUV photon flux at HELIOS is likely to be increased by recoating some of the XUV mirrors, primarily in the monochromator, as they suffered from the 800 nm laser radiation they were exposed to in the beginning of the lab operation. These mirrors have been recoated before but the result could still be improved. The most used grating in the monochromator will be replaced for the same reasons. All these upgrades will allow to use HELIOS more efficiently, freeing lab time and manpower for experiments.

From a scientific point of view, there are numerous experimental areas for HELIOS to be explored. The T-MOKE spectrometer allows investigating element-specific magnetization dynamics of magnetic samples. Beside

measurements on Permalloy and related alloys as $Fe_{1-x}Ni_x$, it is planned to perform measurements on multilayer systems related to superdiffusive spin currents. At the UHV beamline, the ARTOF 2 will allow for a variety of different experiments. Time-resolved photoelectron spectroscopy on solar cell related materials, aiming on investigating charge transfer in donor-acceptor interfaces, is planned to be performed. Alternatively, the setup could e.g. be used for measurements on organic molecules related to photo catalysis. If used for angle-resolved measurement, the ARTOF will e.g. allow for an investigation of the dynamics of correlated materials. Using a gas needle and an electron spectrometer will allow for probing dynamics in gases as e.g. in the photodissociation of O_3.

HELIOS, as described in this thesis, features two beamlines and delivers photon energies up to 72 eV. However, both parameters could potentially be upgraded. The use of zirconium foils instead of aluminum foils in the monochromator would allow for higher photon energies. Attempts with 200 nm thick foils failed but thicker foils in combination with limited laser power for the generation of high harmonics might allow for the transmission of XUV radiation above 72 eV while blocking the driving laser. If it is desired to have the T-MOKE setup as a permanent end station, this setup could be moved to connect to the monochromator directly. Such a configuration is displayed in *Figure 37*. It features a rather large grazing angle of the mirror

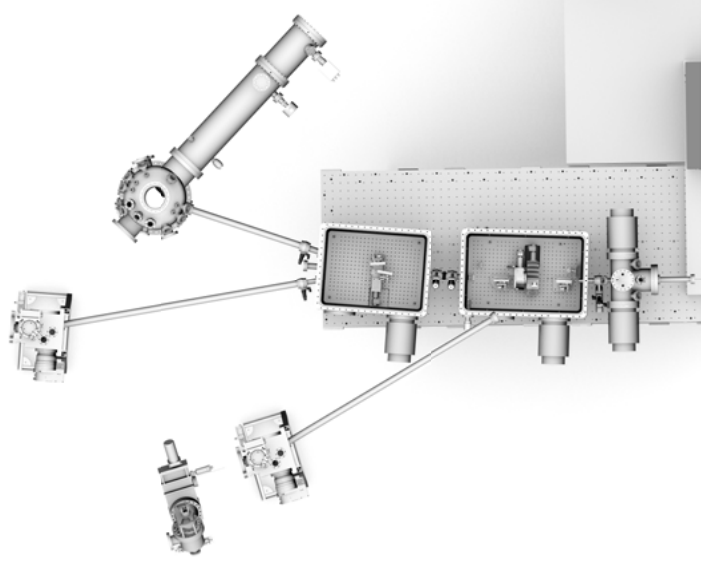

Figure 37. CAD rendering of the T-MOKE spectrometer being connected directly to the monochromator, freeing the µ-focus beamline for other experiments.[44]

in the monochromator but would still provide a reflectivity about equal to the overall reflectivity of the monochromator-beam-routing-chamber beam path currently used. To practically move the T-MOKE beamline in front of the monochromator is an option as this end station does hardly benefit from the monochromator. That way one could free the μ-focus beamline for other activities, while still allowing for fast access to the T-MOKE spectrometer.

The FTS was tested at synchrotron beamlines but it seems not possible yet, to measure any radiation from an emission process of a sample. A main reason for this is that the signal level on the MCP is currently only sufficient to measure XUV radiation reflected from a sample surface. A weak signal is especially problematic as it is additionally spread over large parts of the MCP detector, which leads to a poor signal-to-noise ratio, which in turn is very undesirable for an FTS. Hence, it might be an option to install a refocusing mirror behind the beam mixer to focus the transmitted radiation onto a smaller spot, which should lead to an increase of the signal-to-noise ratio as it reduces the amount of detector noise in the measurement. This method would, though, also lead to some cancelation of the interference signal due to the uneven phase front transmitted by the spectrometer.

8 Populärvetenskaplig sammanfattning

Spektroskopi var en av de viktigaste teknikerna i vetenskapens historia, och var involverad i manga historiska upptäckter. Under en lång tid användes spektroskopi för att undersöka materias statiska egenskaper medan dynamiska processer skedde för snabbt för att kunna undersökas. Dock fanns det alltid ett intresse för tidsupplöst spektroskopi i det vetenskapliga samhället, och tidsupplösningen drevs framåt av den tekniska utvecklingen.

Pulsade lasrar med ett par femtosekunders pulslängder möjliggör användandet av tekniker som kan upplösa processer som också sker på så korta tidsskalor. För att få en ide om hur snabba dessa processer så går det att jämföra följande; en femtosekund förhåller sig till en sekund på samma sätt som en sekund förhåller sig till 32 miljoner år. Dessa processer kan t.ex. vara molekylära vibrationer, kemiska reaktioner, magnetiserings- och fasövergångar. Den mest vanligt förekommande tekniken för tidsupplöst spektroskopi är den så kallade pump-prob tekniken. Här används en ljuspuls (som kallas pump-puls) för att överföra energi till det prov som skall undersökas och för att sätta igång den process som skall studeras. Efter en kort tidsfördröjning så används en annan ljuspuls (som kallas prob-puls) för att göra spektroskopi på provet. Om flera sådana mätningar görs med olika tidsfördröjning så kan man följa processen i tiden. Detta kan jämföras med att lägga samman flera bilder till en film som visar dynamiken i t.ex. en kemisk reaktion.

Pump-probmätningar har gjorts med lasrar i årtionden, dock är de fotonenergier en laser kan ge begränsade till under 7 eV. Denna begränsning i probfotonenergi kan också begränsa den information som probpulsen kan ge, till exempel eftersom detta endast tillåter undersökningar av valensbandet hos ett prov, och ibland endast leder till exciterade elektroner. I kontrast till detta går det, genom att använda laserpulser för att övertonsgenerering (engelska High Harmonic Generation – HHG) att generera probfotoner med mycket högre energi, upp till flera hundra eV. Detta görs genom att fokusera en ultrakort laserpuls (med pulslängd i femtosekundsområdet) i en ädelgas där det skapas fotoner med udda multiplar av den ursprungliga laserfotonens frekvens.

Denna avhandling beskriver HELIOS, ett laboratorium för tidsupplöst spektroskopi med extreme ultraviolett (XUV) strålning skapad i en övertonsgenereringsprocess. HELIOS är baserat på pump-prob-tekniken och har en tidsupplösning på ca. 50 fs. HELIOS byggdes samt driftsattes inom ramen för avhandlingsarbetet och de första experimenten gjordes som visade på dess användbarhet samt potential.

Ett kommersiellt lasersystem som ger 35 fs långa pulser med en våglängd på 800 nm används. Dessa pulser delas sedan upp i två genom en optisk stråldelare. En av dessa två pulser används sedan som pumppuls för att excitera provet eller, om en annan våglängd önskas så kan pulsens våglängd ändras i spannet 235 nm till 20 000 nm via kommersiell utrustning, t.ex. en optisk parametrisk förstärkare. För att bestämma tidsfördröjningen mellan pump- och probpulsen så är ett fördröjningssteg en del av den optiska vägen för pumppulsen, detta kan användas för att ändra väglängden och därför tidsfördröjningen mellan pump- och probpuls.

Den andra pulsen som kommer från stråldelaren fokuseras i en ädelgas för att generera övertoner. Denna XUV strålning kan sen separeras från 800 nm laserstrålningen via en 150 nm till 200 nm tjock aluminiumfolie. Efter denna så finns det övertoner mellan 20 eV och 72 eV kvar, på grund av transmissionen av aluminiumfolien. Eftersom dessa våglängder snabbt absorberas av vilket material som helst likaså av gaser, som luft, så måste hela strålgången för XUV strålningen hållas under vakuum.

En monokromator, placerad efter gascellen, möjliggör att välja endast en liten del av det totala energi/våglängdsområdet hos de genererade övertonerna, denna används slutligen för experiment. Monokromatorn är designad så att den bibehåller en kort pulslängd hos de genererade XUV pulserna, något som inte är vanligt förekommande. Strålningen som passerat monokromatorn kan sen guidas till en av de två existerande strålrören. HELIOS har en halv-permanent experimentstation på ett av strålrören som är tänkt för fotoelektronspektroskopi, även med vinkelupplösning och under ultrahögt vakuum (UHV). En ARTOF 2 vinkelupplösande fotoelektronspektrometer är installerad på detta strålrör. Det andra strålröret slutar med en fokuseringskammare som fokuserar både pump- och probpulsen på provet. Denna kammare kan positioneras relativt flexibelt och kan enkelt anslutas till flertalet experimentstationer, samtidigt som den utgör ett differentiellt pumpsteg för att separera HELIOS från potentiellt höga tryck i experimentkammaren. Detta, och det faktum att XUV-fokuset endast är kring 20 μm i diameter gör detta strålrör idealt för experiment som kräver ett litet XUV fokus, som har höga tryck i experimentkammaren eller som endast är anslutna till HELIOS under en begränsad tid och som kräver extern utrustning.

I den här avhandlingen finns en artikel som beskriver HELIOS-laboratoriet, där beskrivs pump-prob mätningar med 800 nm pumppulser samt XUV strålkning som probe pulser, en tidsupplösning på 50 fs visas. Det visas också att det är möjligt att samtidigt uppnå en energiupplösning på 110 meV vid 41 eV fotonenergi. Funktionaliteten hos UHV experimenten demonstrerades via tids och vinkelupplöst fotoelektronspektroskopimätningar på grafen. För att demonstrera denna uppställnings funktionalitet för tidsupplösta fotoelektronspektroskopiska mätningar utan vinkelupplösning genomfördes en mätning på den ledande polymeren PCPDTBT.

μ-focus strålröret användes för att försöka genomföra tidsupplöst fotoelektronspektroskopi på prover i vätskefas, samt för att genomföra mätningar av magnetiseringsdynamik, i ett permalloyprov, med elementspecificitet. Det senare genomfördes genom att uppgradera en existerande vakuumkammare som redan var utrustad med en elektromagnet. Uppgraderingen bestod i en egenutvecklad provhållare samt en XUV spektrometer. Senna uppställning kan nu användas för att utföra experiment som utnyttjar den transversella magnetooptiska Kerreffekten. Detta är av specifikt intresse då dessa mätningar kan ge information om olika element i ett magnetiskt prov vid en och samma mätning, detta möjliggör mätningar av relativa differenser i de olika ämnenas magnetiseringsdynamik med en tidsupplösning på under 10 fs.

Vid sidan om HELIOS så har en Fouriertransformspektrometer (FTS) för XUV området undersökts i denna avhandling. Det var möjligt att visa att denna spektrometer kunde mäta den infallande strålningens våglängd. Vidare användes denna spektrometer för att mäta den temporära koherensen av den monokromatiserade XUV strålningen vid HELIOS.

9 Acknowledgements

The last years would not have been possible nor worthwhile without the presence of a lot of people. Only those people make physics more than a subject of dead matter in artificial surroundings.

First of all I want to thank my supervisor Johan S. for five years of pleasant work with a very interesting project and for always having a cheering word and time for fruitful discussions. His interest in lab activities and the well-being of his surroundings made work a great place to be at. I want to thank Marcus for three fun FTS beam times, for all the LabVIEW knowledge I stole from him and for always having solid answers to solid problems. I very much appreciated having co-supervisors as Ruben and Hans who were available for the questions which needed a lot of experience and overview. Thank you very much for that. And thank you, Ruben, for accepting me as a project student about six years back. You are actually the reason why I ended up in this division.

I would like to thank all the members of the division of molecular and condensed matter physics for making it such a great place to work at. For all the help one gets, may it be intellectual or physical, for all the interesting discussions at lunch or fika and the occasional outside work activities. Many thanks also go to all who were lab assistances with me and tried to teach students physics, whether the students wanted or not. Special thanks go to Rein, who represents the good spirit of the division and often has what one needs before one even knows oneself.

Working at university means that one works closely with a lot of people. I would like to thank all of them, may it be that we met on beam times or that we worked together in HELIOS. I would like to express my special gratitude towards Mattias, Nils and Robert who worked at HELIOS as postdocs and with whom I shared a lot of fun lab hours of interesting discoveries as well as frustrating endeavors. My thanks also go to Somnath for teaching me magnetism and Indian culture as well as to Ute for investing so much time into HELIOS and scientific discussions. Special thanks go to Stefan for all the nice drawings he made which became HELIOS and which were the base of my work to build upon, for introducing me to HELIOS and for helping with it thereafter, but also for letting me to glimpse into the world of engineering. There is a lot I learned from you.

I would also like to thank the Ångström workshop and its employees for all the help I received and I would like to express my special gratitude to Eric, who was always available to deliver the finest parts and solutions in a minimum of time. Many thanks go to Anders O., who gave me some insight into the world of 3D printing and made it easy to share his grounded enthusiasm for it. I also thank the administration of the department of physics and astronomy, especially Anne and Inger for all the uncomplicated handling of dozens of invoices, countless days of parental leave and quite a number of new contracts.

My PhD in physics took less than five years, but I was taught physics for about twelve years before. I would like to express my gratitude towards everyone from whom I learned during this time, especially to my high-school teachers in physics and math who laid the foundations for my studies, my learning group during my studies who made physics a fun science and to my supervisors at that time who introduced me to lab work.

Last but not least I would like to thank all my friends in Uppsala for making it a great place to be at. Thank you, Daniel, Fredrik, Josephina, Li, Sebastian and Tove, for a lot of shared food, games and the pleasant company making them worthwhile and all the time you invested in serving Paula with whatever she desired of you. Thank you, Sabrina and Stefan, for all the food you served for us, for the board games we played and the general support in Sweden. I would also like to express my special gratitude to Sabrina for allowing me to work on my PhD while knowing that Paula is in the best hands.

I would like to thank all my friends in Germany for the invitations when we were on holiday, for numerous phone calls and a lot of visits. It will make foreign grounds look much nicer if you still have contact to your homeland. I would also like to thank my parents-in-law for a number of visits and for allowing us to spend a big part of the overall relaxing time on holidays in their company. Big thanks go to my family, who visited us so often and supported us so nicely with foreign supplies, who was always available to enable our holidays and to cheer Paula and who supported us so much with whatever was needed, whether it was advice or action. Thank you so much!

And thank you, Carla, for making this time a time to look back on knowing that it was not wasted, no matter what will come in the future. Paula, whenever you read this, you can find out above why I went out every day, but you should know that it was you who always gave me a reason to leave for home.

10 References

1. Gordon, G. & Cady, W. M. An Apparatus for Time-Resolved Spectroscopy. *J. Opt. Soc. Am.* **40,** 852–853 (1950).
2. Mauritsson, J. *et al.* Attosecond electron spectroscopy using a novel interferometric pump-probe technique. *Phys. Rev. Lett.* **105,** 053001–1 – 053001–4 (2010).
3. Joachim Terschluesen, Pump probe setup.svg (https://commons.wikimedia.org/wiki/File:Pump_probe_setup.svg) Licenced under CC0 1.0 (https://creativecommons.org/publicdomain/zero/1.0/deed.en).
4. McPherson, A. *et al.* Studies of multiphoton production of vacuum-ultraviolet radiation in the rare gases. *J. Opt. Soc. Am. B* **4,** 595–601 (1987).
5. Siegbahn, H. & Karlsson, L. Photoelectron Spectroscopy. *Springer-Verlag* (1982).
6. Agåker, M. *et al.* Novel instruments for ultra-soft X-ray emission spectroscopy. *Nucl. Instruments Methods Phys. Res. Sect. A Accel. Spectrometers, Detect. Assoc. Equip.* **601,** 213–219 (2009).
7. Cerullo, G. & De Silvestri, S. Ultrafast optical parametric amplifiers. *Rev. Sci. Instrum.* **74,** 1–18 (2003).
8. Kanal, F., Keiber, S., Eck, R. & Brixner, T. 100-kHz shot-to-shot broadband data acquisition for high-repetition-rate pump–probe spectroscopy. *Opt. Express* **22,** 16965–16975 (2014).
9. Fischbach, S., Gorbach, A. V., Di Nuzzo, D. & Da Como, E. Near infrared ultrafast pump-probe spectroscopy with ZrF4-BaF2-LaF3-AlF3-NaF fiber supercontinuum. *Appl. Phys. Lett.* **107,** 021103–1 – 021103–4 (2015).
10. Winterfeldt, C., Spielmann, C. & Gerber, G. Colloquium: Optimal control of high-harmonic generation. *Rev. Mod. Phys.* **80,** 117–140 (2008).
11. Popmintchev, T., Chen, M.-C., Arpin, P., Murnane, M. M. & Kapteyn, H. C. The attosecond nonlinear optics of bright coherent X-ray generation. *Nat. Photonics* **4,** 822–832 (2010).
12. Sandberg, R. L. *et al.* Lensless diffractive imaging using tabletop coherent high-harmonic soft-X-ray beams. *Phys. Rev. Lett.* **99,** 098103–1 – 098103–4 (2007).
13. Ravasio, A. *et al.* Single-shot diffractive imaging with a table-top femtosecond soft X-ray laser-harmonics source. *Phys. Rev. Lett.* **103,** 028104–1 – 028104–5 (2009).
14. Bergeard, N. *et al.* Time-resolved photoelectron spectroscopy using synchrotron radiation time structure. *J. Synchrotron Radiat.* **18,** 245–250 (2011).
15. Plogmaker, S. *et al.* Versatile high-repetition-rate phase-locked chopper system for fast timing experiments in the vacuum ultraviolet and x-ray spectral region. *Rev. Sci. Instrum.* **83,** 013115–1 – 013115–6 (2012).

16. Sun, C., Portmann, G., Hertlein, M., Kirz, J. & Robin, D. S. Pseudo-single-bunch with adjustable frequency: A new operation mode for synchrotron light sources. *Phys. Rev. Lett.* **109,** 264801–1 – 264801–5 (2012).
17. Holldack, K. *et al.* Single bunch X-ray pulses on demand from a multi-bunch synchrotron radiation source. *Nat. Commun.* **5,** 4010 1–7 (2014).
18. Khan, S., Holldack, K., Kachel, T., Mitzner, R. & Quast, T. Femtosecond Undulator Radiation from Sliced Electron Bunches. *Phys. Rev. Lett.* **97,** 074801–1 – 074801–4 (2006).
19. Schoenlein, R. W. *et al.* Generation of femtosecond pulses of synchrotron radiation. *Science (80-.).* **287,** 2237–2240 (2000).
20. Winick, H., Brown, G., Halbach, K. & Harris, J. Wiggler and Undulator Magnets. *Phys. Today* **34,** 1–14 (1981).
21. McNeil, B. W. J. & Thompson, N. R. X-ray free-electron lasers. *Nat. Photonics* **4,** 814–821 (2010).
22. Allaria, E. *et al.* Highly coherent and stable pulses from the FERMI seeded free-electron laser in the extreme ultraviolet. *Nat. Photonics* **6,** 699–704 (2012).
23. Amann, J. *et al.* Demonstration of self-seeding in a hard-X-ray free-electron laser. *Nat. Photonics* **6,** 693–698 (2012).
24. Mancuso, A. P., Yefanov, O. M. & Vartanyants, I. A. Coherent diffractive imaging of biological samples at synchrotron and free electron laser facilities. *J. Biotechnol.* **149,** 229–237 (2010).
25. Chapman, H. N. *et al.* Femtosecond diffractive imaging with a soft-X-ray free-electron laser. *Nat. Phys.* **2,** 839–843 (2006).
26. Lewenstein, M., Balcou, P., Ivanov, M. Y., L'Huillier, A. & Corkum, P. B. Theory of high-harmonic generation by low-frequency laser fields. *Phys. Rev. A* **49,** 2117–2132 (1994).
27. Kfir, O. *et al.* Generation of bright phase-matched circularly-polarized extreme ultraviolet high harmonics. *Nat. Photonics* **9,** 99–105 (2014).
28. Plogmaker, S. *et al.* HELIOS—A laboratory based on high-order harmonic generation of extreme ultraviolet photons for time-resolved spectroscopy. *Rev. Sci. Instrum.* **86,** 123107 (2015).
29. Paul, A. *et al.* Quasi-phase-matched generation of coherent extreme-ultraviolet light. *Lett. to Nat.* **421,** 51–54 (2003).
30. Plogmaker, S. Techniques and Application of Electron Spectroscopy Based on Novel X-ray Sources. *Uppsala Univ.* **903,** (2012).
31. Berkeley Lab - CXRO - X-Ray interaction - Mirror Reflectivity. Date Accessed 02 March 2016 at <http://henke.lbl.gov/optical_constants/mirror2.html>
32. Berkeley Lab - CXRO - X-Ray interaction - Filter Transmission. Date Accessed 02 March 2016 at <http://henke.lbl.gov/optical_constants/filter2.html>
33. Seah, M. P. & Dench, W. A. Quantitative Electron Spectroscopy of Surfaces : A Standard Data Base for Electron Inelastic Mean Free Paths in Solids. *Surf. Interface Anal.* **1,** 2–11 (1979).
34. Demtröder, W. *Experimentalphysik 3*. (Springer, 2005).
35. Joachim Terschluesen, Diffraction from a blazed grating.svg (https://commons.wikimedia.org/wiki/File:Diffraction_from_a_blazed_grating.svg) Licenced under CC0 1.0 (https://creativecommons.org/publicdomain/zero/1.0/deed.en).

36. Villoresi, P. Compensation of optical path lengths in extreme-ultraviolet and soft-x-ray monochromators for ultrafast pulses. *Appl. Opt.* **38,** 6040–6049 (1999).
37. Poletto, L. & Frassetto, F. Time-preserving grating monochromators for ultrafast extreme-ultraviolet pulses. *Appl. Opt.* **49,** 5465–5473 (2010).
38. Frassetto, F. *et al.* Design and characterization of the XUV monochromator for ultrashort pulses at the ARTEMIS facility. *Proc. SPIE* **7077,** 707713–1 – 707713–10 (2008).
39. Joachim Terschluesen, Diffraction of a short pulse on a grating.svg (https://commons.wikimedia.org/wiki/File:Diffraction_of_a_short_pulse_on_a_grating.svg) Licenced under CC0 1.0 (https://creativecommons.org/publicdomain/zero/1.0/deed.en).
40. Bell, R. J. *Introductory Fourier Transform Spectroscopy*. (Academic Press, 1972).
41. Thorne, A. High resolution Fourier transform spectrometry in the visible and ultraviolet regions. *J. Anal. At. Spectrom.* **13,** 407–411 (1998).
42. Joachim Terschluesen, Fourier Transform spectrometer principle.svg (https://commons.wikimedia.org/wiki/File:Fourier_Transform_spectrometer_principle.svg) Licenced under CC0 1.0 (https://creativecommons.org/publicdomain/zero/1.0/deed.en).
43. Griffiths, P. R. & De Haseth, J. A. *Fourier Transform Infrared Spectrometry*. (Wiley, 2007).
44. CAD rendering based on drawings from Plogmaker, S. & Södergren, S. & Johansson, N. & Scienta.
45. Han-Kwang Nienhuys, CPA compressor.svg (https://en.wikipedia.org/wiki/File:CPA_compressor.svg) Licenced under CC BY 2.5 (http://creativecommons.org/licenses/by/2.5/#).
46. Verluise, F., Laude, V., Cheng, Z., Spielmann, C. & Tournois, P. Amplitude and phase control of ultrashort pulses by use of an acousto-optic programmable dispersive filter: pulse compression and shaping. *Opt. Lett.* **25,** 575 (2000).
47. Kaplan, D. & Tournois, P. Theory and performance of the acousto optic programmable dispersive filter used for femtosecond laser pulse shaping. *J. Phys. IV* **12,** 69–75 (2002).
48. Raman fastlite, AOPDF_principle.png (https://commons.wikimedia.org/wiki/File:AOPDF_principle.png) Licenced under CC BY-SA 3.0 (http://creativecommons.org/licenses/by-sa/3.0/).
49. RefractiveIndex.info. *Main - Gold - Babar Weav. 2015* Date Accessed 04 March 2016 at <http://refractiveindex.info/?shelf=main&book=Au&page=Babar>
50. RefractiveIndex.info. *Main - Gold - Olmon 2012 Evaporated gold* Date Accessed 04 March 2016 at <http://refractiveindex.info/?shelf=main&book=Au&page=Olmon-ev>
51. CAD rendering based on drawings from Södergren, S.
52. Öhrwall, G. *et al.* A new energy and angle resolving electron spectrometer - First results. *J. Electron Spectros. Relat. Phenomena* **183,** 125–131 (2011).
53. Scienta Omicron. ARTOF-2 technical data. Date Accessed 23 March 2016 at <http://www.scientaomicron.com/en/products/358/1224>
54. CAD rendering based on drawings from Johansson, N. & Scienta.
55. Horn-von Hoegen, M. Growth of semiconductor layers studied by spot profile analysing low energy electron diffraction. *Zeitschrift fur Krist.* **214,** 684–721 (1999).

56. de Oliveira, N. *et al.* High-resolution broad-bandwidth Fourier-transform absorption spectroscopy in the VUV range down to 40 nm. *Nat. Photonics* **5,** 149–153 (2011).
57. Balasubramanian, T. *et al.* The normal incidence monochromator beamline I3 on MAX III. *AIP Conf. Proc.* **1234,** 661–664 (2010).
58. Agåker, M. *et al.* Spectroscopy in the vacuum-ultraviolet. *Nat. Photonics* **5,** 248–248 (2011).
59. Terschlüsen, J. A. *et al.* Measuring the temporal coherence of a high harmonic generation setup employing a Fourier transform spectrometer for the VUV/XUV. *Nucl. Instruments Methods Phys. Res. Sect. A* **768,** 84–88 (2014).
60. Berger, C. *et al.* Ultrathin Epitaxial Graphite: 2D Electron Gas Properties and a Route toward Graphene-based Nanoelectronics. *J. Phys. Chem. B* **108,** 19912–19916 (2004).
61. Johannsen, J. C. *et al.* Direct View of Hot Carrier Dynamics in Graphene. *Phys. Rev. Lett.* **111,** 027403 (2013).
62. Peet, J. *et al.* Efficiency enhancement in low-bandgap polymer solar cells by processing with alkane dithiols. *Nat. Mater.* **6,** 497–500 (2007).
63. Mühlbacher, D. *et al.* High Photovoltaic Performance of a Low-Bandgap Polymer. *Adv. Mater.* **18,** 2884–2889 (2006).
64. Fazzi, D. *et al.* Ultrafast internal conversion in a low band gap polymer for photovoltaics: experimental and theoretical study. *Phys. Chem. Chem. Phys.* **14,** 6367–6374 (2012).
65. Grancini, G. *et al.* Hot exciton dissociation in polymer solar cells. *Nat. Mater.* **12,** 29–33 (2013).
66. Albrecht, S. *et al.* On the field dependence of free charge carrier generation and recombination in blends of PCPDTBT/PC70BM: influence of solvent additives. *J. Phys. Chem. Lett.* **3,** 640–645 (2012).
67. Clarke, T. *et al.* Transient absorption spectroscopy of charge photogeneration yields and lifetimes in a low bandgap polymer/fullerene film. *Chem. Commun.* **7345,** 89–91 (2009).
68. Rao, A. *et al.* The role of spin in the kinetic control of recombination in organic photovoltaics. *Nature* **500,** 435–440 (2013).
69. Morana, M. *et al.* Nanomorphology and charge generation in bulk heterojunctions based on low-bandgap dithiophene polymers with different bridging atoms. *Adv. Funct. Mater.* **20,** 1180–1188 (2010).
70. Mathias, S. *et al.* Probing the timescale of the exchange interaction in a ferromagnetic alloy. *Proc. Natl. Acad. Sci. U. S. A.* **109,** 4792–4797 (2012).
71. Höchst, H., Rioux, D., Zhao, D. & Huber, D. L. Magnetic linear dichroism effects in reflection spectroscopy: A case study at the Fe M2,3 edge. *J. Appl. Phys.* **81,** 7584–7588 (1997).
72. Joachim Terschluesen, Transverse magneto-optic Kerr effect (T-MOKE) geometry.svg (https://commons.wikimedia.org/wiki/File:Transverse_magneto-optic_Kerr_effect_%28T-MOKE%29_geometry.svg) Licenced under CC0 1.0 (https://creativecommons.org/publicdomain/zero.
73. Rudolf, D. *et al.* Ultrafast magnetization enhancement in metallic multilayers driven by superdiffusive spin current. *Nat. Commun.* **3,** 1037 (2012).
74. Mathias, S. *et al.* Ultrafast element-specific magnetization dynamics of complex magnetic materials on a table-top. *J. Electron Spectros. Relat. Phenomena* **189,** 164–170 (2013).
75. La-O-Vorakiat, C. *et al.* Ultrafast demagnetization dynamics at the M edges of magnetic elements observed using a tabletop high-harmonic soft X-ray source. *Phys. Rev. Lett.* **103,** 257402–1 – 257402–4 (2009).

76. Neuhauser, R. E., Ferstl, B., Haisch, C., Panne, U. & Niessner, R. Design of a low-cost detection system for laser-induced plasma spectroscopy. *Rev. Sci. Instrum.* **70,** 3519–3522 (1999).
77. Malacara, D. *Geometrical and Instrumental Optics*. (Academic Press, INC. London LTD., 1988).
78. Troisi, S. Testing and First Applications of a Spectrometer for Time-Resolved T-MOKE Measurements. *Uppsala Univ.* (2016).
79. Bergersen, H. *et al.* A photoelectron spectroscopic study of aqueous tetrabutylammonium iodide. *J. Phys. Condens. Matter* **19,** 326101 (2007).
80. Werner, J. Exploring the Surface of Aqueous Solutions. *Uppsala Univ.* **1313,** 35 (2015).
81. Lindblad, A. A Treatise on the Geometric and Electronic Structure of Clusters. *Uppsala Univ.* **393,** 53 (2008).
82. Samson, J. A. R. Angular Distribution of Photoelectrons. *J. Opt. Soc. Am.* **59,** 356–357 (1969).
83. Reilman, R. F., Msezane, A. & Manson, S. Relative Intensities in Photoelectron Spectroscopy of Atoms and Molecules. *J. Electron Spectros. Relat. Phenomena* **8,** 389–394 (1976).

Acta Universitatis Upsaliensis

Digital Comprehensive Summaries of Uppsala Dissertations from the Faculty of Science and Technology 1360

Editor: The Dean of the Faculty of Science and Technology

A doctoral dissertation from the Faculty of Science and Technology, Uppsala University, is usually a summary of a number of papers. A few copies of the complete dissertation are kept at major Swedish research libraries, while the summary alone is distributed internationally through the series Digital Comprehensive Summaries of Uppsala Dissertations from the Faculty of Science and Technology. (Prior to January, 2005, the series was published under the title "Comprehensive Summaries of Uppsala Dissertations from the Faculty of Science and Technology".)

Distribution: publications.uu.se
urn:nbn:se:uu:diva-281298

ACTA
UNIVERSITATIS
UPSALIENSIS
UPPSALA
2016